SCUOLA DI SCIENZE
Dipartimento di Chimica Industriale "Toso Montanari"

Corso di Laurea Magistrale in
Chimica Industriale
Curriculum: Advanced Spectroscopy in Chemistry
Classe LM-71 - Scienze e Tecnologie per la Chimica Industriale

Excited State Energy Surfaces of Flexible Emitters for Thermally Activated Delayed Fluorescence

CANDIDATE

Panukorn Sombut

SUPERVISOR

Dr. Luca Muccioli

CO-SUPERVISOR

Prof. Roberto Berardi

Dr. Silvia Orlandi

Prof. Alberto Arcioni

Lorenzo soprani

Session I

Academic Year 2018/2019

University of Bologna

Faculty of Science

Industrial Chemistry Department

Erasmus Mundus Joint Master Degree

"Advanced Spectroscopy in Chemistry"

MASTER THESIS

by

Panukorn Sombut

Excited state energy surfaces of flexible emitters for Thermally Activated Delayed Fluorescence

Research group: liquid crystal

Supervisor(s): Dr. Luca Muccioli

Reviewer(s): Prof. Artur Michalak

Acknowledgement

I would like to express my sincerest gratitude to my supervisor for the guidance, encouragement and advice during my time working with him. His enthusiasm for research has motivated me with no end to continue in research. The master thesis project "Excited state energy surfaces of flexible emitters for Thermally Activated Delayed Fluorescence" with the help of my master thesis supervisor Dr.Luca Muccioli turned out to be a great success!

I also wish to truly give a big thanks to my co-advisors: Prof. Roberto Berardi, Dr. Silvia Orlandi and Prof. Alberto Arcioni whose involvement in this master thesis. Dr. Silvia Orlandi was exceptionally helpful for me with the time spent proofreading my writing of the thesis and helping to correct it.

Moreover, I would like to thank you to Dr.Yoann Olivier for helpful suggestions throughout my work. And also, Prof. Artur Michalak who is the external evaluator, to review and give feedback my master thesis.

Throughout the time I worked on my master thesis, I was also fortunate to receive some guidance from people in the lab. Therefore, I would like to thank the PostDocs in the group, Davide Presti who helped me with spin-orbit coupling calculation, and also Lara Querciagrossa who worked with me to read through my thesis and offer her valuable advice whenever I had a question. I would also to thank a PhD student Lorenzo Soprani who took care of me during the time I have worked in this project.

Last but not least, I would like to give a massive "thank you" to the Advanced Spectroscopy in Chemistry programme who have set me up for life and provided me this enormous opportunity to pursue my research career.

Panukorn Sombut

ABSTRACT:

Organic Light-Emitting Diodes (OLEDs) technology has matured over recent years, reaching the commercialization level and being used in various applications. The required efficiency can be achieved by transforming triplet excitons into singlet states via Reverse InterSystem Crossing (RISC), which a general mechanism called thermally activated delayed fluorescence (TADF). Two prototypical molecules in the field, 2CzBN and 4CzBN, Carbazole Benzonitrile (donor- acceptor) derivatives, possess similar energy gap between singlet and triplet (ΔE_{ST}, a key parameter in the RISC rate), but different TADF performance. In this sense, other parameter must be considered to explain these different behaviors.

In this work, we theoretically investigate 2CzBN and 4CzBN and address the problem of how flexible donor-acceptor (D-A) or donor-acceptor-donor (D-A-D) molecular architectures affect the nature of excited state, and the oscillator strength. Furthermore, we analyze the RISC rates as a function of the conformation of the carbazole side groups, considering the S_0, S_1, T_1 and T_2 states. The oscillator strength of 4CzBN is higher than of 2CzBN, which, in turn, is almost vanishing, resulting in only 4CzBN being a TADF active molecule. We also note the presence of a second triplet state T_2 lower in energy than S_1, and that the reorganization energies, associated to the RISC processes involving T_1 and T_2, are both important factor in differentiating the rates in 2CzBN and 4CzBN. However, the 4CzBN RISC rate from T_2 to S_1 is surprisingly high with respect to the one from T_1 to S_1, although, according to EL-Sayed rules, since T_2 (CT/LE) is more similar to S_1 (CT) than in 2CzBN (LE, CT), this transition should be less favored. These insights are important to understand the photophysics of the TADF process and to design novel TADF emitters based on the benzo-carbazole architecture.

4

Contents

List of Abbreviations

2CzBN = 2,3-di(9H-carbazol-9-yl)benzonitrile

4CzBN = 2,3,5,6-tetra(9H-carbazol-9-yl)benzonitrile

A= Acceptor group

D= Donor group

DF = Delayed florescence

EIL =electron-injection layers

EML = emitting layer

ETL = electron-transporting layer

HIL = Hole-injection layer

HOMO =Highest Occupied Molecular Orbital

HTL = hole-transporting layer

ISC = Intersystem crossing

LUMO= Lowest Unoccupied Molecular Orbital

NTO = Natural Transition Orbitals

OLEDs = organic light emitting diodes

PF = Prompt florescence

RISC = Reverse intersystem crossing

S_0 = first ground state

S_1 = first single excited state

S_2 = second single excited state

SOC = Spin-orbit coupling

T_1 = first triplet excited state

T_2= second triplet excited state

TADF = Thermally Activated Delayed Florescence

Chapter 1

Introduction

a   b
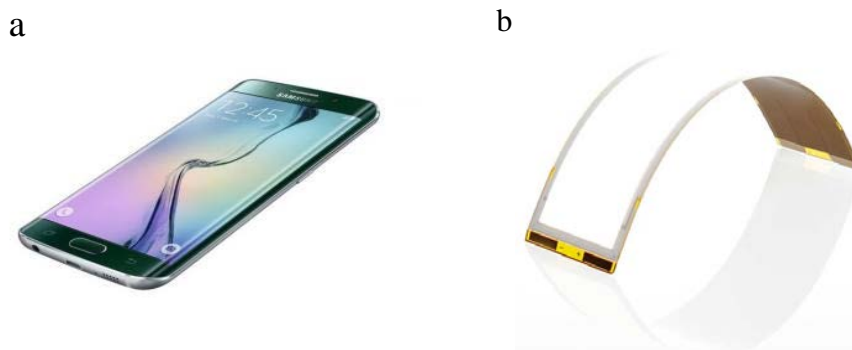
Figure 1.1 Examples of present organic semiconductor applications a) OLEDs display in the Galaxy smartphone series by Samsung and b) OLED-based lighting panel.

Organic Light-Emitting Diodes (OLEDs) technology has matured over recent years, reaching the commercialization level and being used in various applications, such as lighting panels and mobile displays (figure 1.1)[1]. The world's first working OLED, consisting of a double-layers structure of organic thin films was developed by Ching W. Tang and Steven Van Slyke in 1987[2]. Nowadays, OLED emitters consist of many organic layers stacking between anode and cathode as shown in figure 1.2. In all types of devices, hole/electron injection layers (HIL/EIL) are used to ease charge injection, and hole/electron transporting layers (HTL/ETL) bring the charge carriers to the emitting layer (EML), which is used for light emission[3]. These electrons and holes travel through the semiconductor, before encountering each other and forming a strongly bound electron-hole pair, called exciton by physicists, or excited state in a more chemical language, implying its full localization in a single molecular unit.
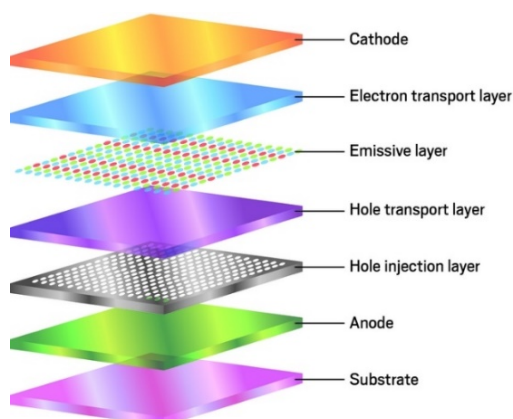
Figure 1.2 Multi-layer structure employed in current OLED products.

The physical processes exploited to generate light from these excitons are multiple. In fact, due to the limit of spin statistics combination, only 25% of current-generated excitons are singlet states, for which selection rules for electronic transitions allow the emissive decay to the singlet ground state. If only this mechanism is in play, known as prompt fluorescence (PF), it sets the theoretical limit of Internal Quantum Efficiency (IQE) to 25 %. The 75 % of triplet excitons are generally non-emissive due to the spin forbidden transition from T_1 to S_0[4]. Also the spin-flip from pure S_1 to pure T_1 states via intersystem crossing (ISC) is forbidden due to their difference in spin multiplicities, but it becomes possible when their wave functions are mixed through spin-orbit coupling (SOC)[5,6]. By including a heavy metal such as Iridium or Platinum into an organic molecule, SOC is enhanced and a strong mixing of spin orbitals in S and T states takes place, resulting in an efficient $S_1 \rightarrow T_1$ conversion and in the ensuing phosphorescence process (from T_1 to S_0 states) with nearly 100 % of IQE. Recent metal-based OLED emitters can be reach External Quantum Efficiency (EQE) close to 30 %[7]. However, the stability of metal-based OLEDs in the blue emission region still needs to be improved[8]. Moreover, the drawback of using rare metal-based materials is that they are highly costly and toxic. Recently, a new design for fully organic emitters that exhibit a phenomenon known as Thermally Activated Delayed Fluorescence (TADF) has been adopted. The concept of TADF is not new as it was first rationalized in solid uranyl salts by Perrin in 1929[9]. TADF is based on a thermally activated reverse (up-conversion) intersystem crossing (RISC) from the lowest triplet (T_1) excited state to the lowest singlet (S_1) excited state, leading to a delayed Fluorescence (DF) (figure 1.3). Consequently, the IQE can easily reach up to 100 %. However, TADF based OLEDs have performances still unsatisfactory in the red and blue regions, and also have a broad emission spectrum[10,11]. Instead, to achieve high color purity in display applications, a narrow emission is required[12]. To achieve high efficiency, TADF emitters should have a fast radiative decay, but also a small energy gap between S_1 and T_1 to promote the RISC process. A small ΔE^{ST} can be realized by CT intramolecular excitations from the ground state, a strategy that, in practice, minimizes the exchange energy of excited state S_1 and brings its energy close to the one of the triplet state T_1. Unfortunately, to achieve a CT character the wavefunctions of S_0 and S_1 (and T_1) must be, as much as possible, localized in different regions of the molecule, and this also minimizes the S_0-S_1 transition dipole and leads to molecules with small radiative rates. In this regard, Monkman and co-workers suggested a key role of the presence of a locally excited triplet state (^{3}LE) in near resonance with charge transfer (CT) states, which might lead to an improvement of the interconversion mechanism[13]. To date, the

full understanding of photophysics of TADF mechanism is still under debate and needs to be achieved in order to optimize device performance.
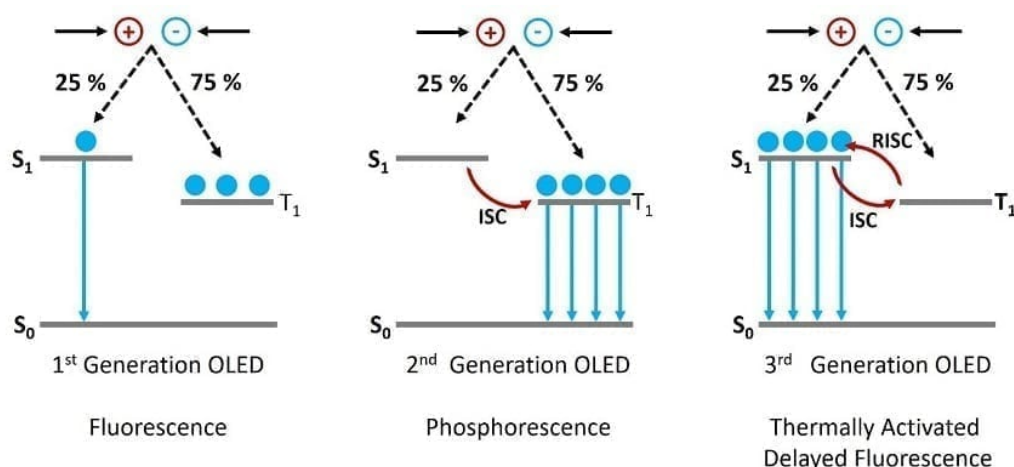
Figure 1.3 The evolution of the strategies for obtaining light emission in Organic Light-Emitting Diodes (OLEDs).

In a one-electron excitation picture, the strategy to harvest the non-radiative exciton in triplet to singlet via RISC is to minimize the spatial overlap between the Highest Occupied Molecular Orbital (HOMO) and Lowest Unoccupied Molecular Orbital (LUMO), leading singlet and triplet first excited states close in energy. The most common molecular design of TADF emitter then consists in covalently linked donor and acceptor moieties that efficiently confine hole and electron densities over different spatial regions[14]. The formation of excited states with strong CT character leads to a reduced overlap between the HOMO and LUMO, resulting in a small ΔE^{ST}[15]. However, the presence of donor and acceptor groups is not a sufficient condition to minimize ΔE^{ST}, but it is also required a near-orthogonal geometry between them to avoid extended conjugation[16]. Therefore, the dihedral angles between donor (D) and acceptor (A) moieties also play an important role in TADF emitters, and they can significantly vary among regioisomers of the same emitter. Additionally, the small ΔE^{ST} is not the only parameter to explain an efficient RISC. It is worth stressing again that recent literature also addresses the presence of the spin-vibronic coupling and the mixing of charge transfer and localized excitation states to be beneficial to RISC[17].

In this study, we theoretically investigate two selected Carbazole Benzonitrile derivatives, which are 2,3-di(9*H*-carbazol-9-yl)benzonitrile (2CzBN) and 2,3,5,6-tetra(9*H*-carbazol-9-yl)benzonitrile (4CzBN) synthesized by Adachi and co-workers[18]. Carbazole plays

the role of the electron donating group while benzonitrile exhibits as the electron accepting group. These molecules are a good example to compare TADF in molecules with D-A and D-A-D architecture. From the experimental results, despite their apparent chemical similarity, 2CzBN is a TADF inactive emitter while 4CzBN is TADF active. Therefore, 2CzBN and 4CzBN are theoretically studied and the TADF mechanism dissected with DFT and TD-DFT calculations. We will address the problem of how flexible donor-acceptor or donor-acceptor-donor molecular architectures affect the nature of excited state and of the RISC rates, which play a key role in the TADF process.

This thesis is organized as follows: in Chapter 2 a more detailed description of TADF-based OLEDs and of the challenge of designing TADF is given. The details of the electronic structure of 2CzBN and 4CzBN are given in Chapter 3. In Chapter 4, we characterize the nature of excited state and of their crossings. The conclusions are drawn in Chapter 5.

Chapter 2

Background

This chapter provides a photophysical background of the main electronic processes governing thermally activated delayed fluorescence, with particular focus on its application on organic light emitting diodes.

2.1 Organic Light Emitting Diodes (OLEDs)
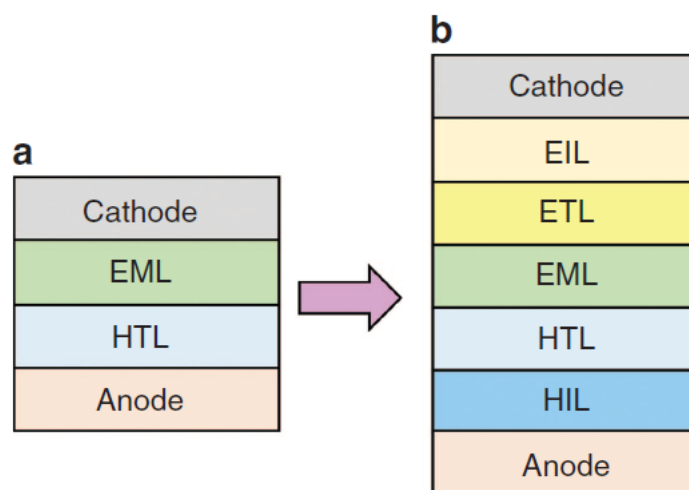
Figure 2.1.1 Schematic diagram of an OLED. (a) Basic structure proposed by Tang and VanSlyke in 1987. (b) Multi-layer structure employed in current OLED products. Figure adapted from reference 3.

The basic structure of an OLED emitter was first proposed by Tang and VanSlyke in 1987[2]. It consists of two layers of organic thin films, an emitting layer (EML) and a hole-transporting layer (HTL), sandwiched between anode and cathode (where the anode layer is next to the glass substrate layer), as shown in Figure 2.1.1a. Electrons and holes are injected from the electrodes to organic layers for recombination and light emission. Nowadays, multi-layer structures in OLEDs with different functional materials are commonly used, as shown in Figure 2.1.1b. The emitting layer (EML), which is used for light emission, consists of dopant and host materials with high quantum efficiency and high carrier mobility. Hole-transporting layer (HTL) and electron-transporting layer (ETL) between the EML and electrodes bring

carriers into the EML for recombination. Hole- and electron-injection layers (HIL and EIL) are inserted between the electrodes and the HTL and ETL interface to facilitate carrier injection from the conductors to the organic layers via an energy level cascade. When voltage is applied to the OLED, electrons and holes supplied from the cathode and anode, respectively, migrate to the EML for recombination to give light[1].

2.2 Carbazole-based materials as TADF emitters
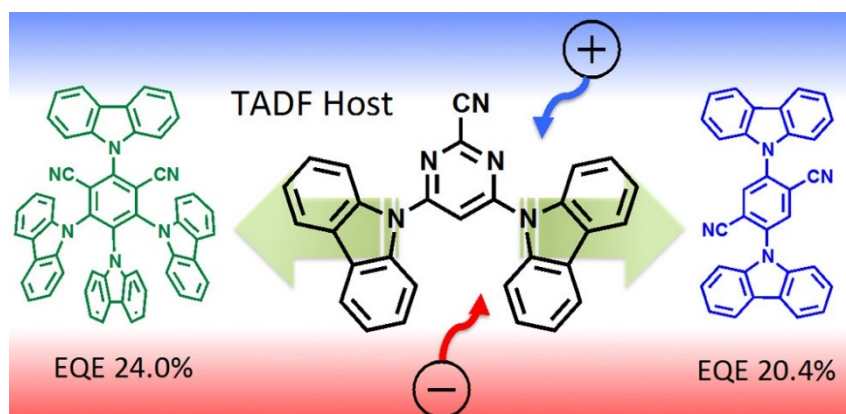
Figure 2.2.1 Cyanopyrimidine-Carbazole derivative for hybrid host material for high external quantum efficiency of TADF-based OLEDs emitter where 4CzIPN is a green emitter (left) and 2CzIPN is a blue emitter (right). Figure adapted from reference 19.

Carbazole has been widely used toward optoelectronic device applications as a source for host materials and emitters[20]. It is an excellent hole-transporter, and also a good electron transporter when substituted with electron withdrawing groups. Many researchers who conduct their research in a field of TADF-based OLEDs have used carbazole with other electron acceptor groups, as carbazole exhibits strong electron donating properties. Carbazole have been widely used as an organic material in optoelectronic device because is an inexpensive starting material. It also contains a nitrogen atom which eases functionalization and thus property modification without altering the backbone, as well as linkage positions on 2, 3, 6, 7 on the carbazole backbone. Moreover, the aromatic properties confer stability under a wide range of conditions.

2.3 Singlet and Triplet states

In organic molecules, the electronic ground state is generally a singlet state where two electrons occupy a single orbital and have antiparallel paired spins. In excited states, one electron is promoted to an orbital with higher energy, leading to two unpaired electrons in different orbitals with antiparallel (singlet states) or parallel (triplet states) spins.

In an electroluminescence process, the excitons in the emission layer of an OLEDs are generated via a recombination of (negatively charged) electrons and (positively charged) holes. Since both holes and electrons have unpaired spins, their combination can give rise to a singlet exciton and to three triplet excitons[4]. According to quantum mechanics, the spin angular momentum **S** is a vector quantity, sum of all individual electron spins, whereas spin multiplicity (m, the number of possible states for a given value of S) is given by m=2S+1. A two-electron system will have four possible spin eigenstates (Figure 2.3.1), one combination of antiparallel spins, giving a singlet (S=0, m=1), and three combinations of parallel spins, giving a triplet (S=1, m=3). Therefore, only 25 % of the excitons formed in an OLED are represented by singlets, and 75 % by triplets, due to spin statistics.
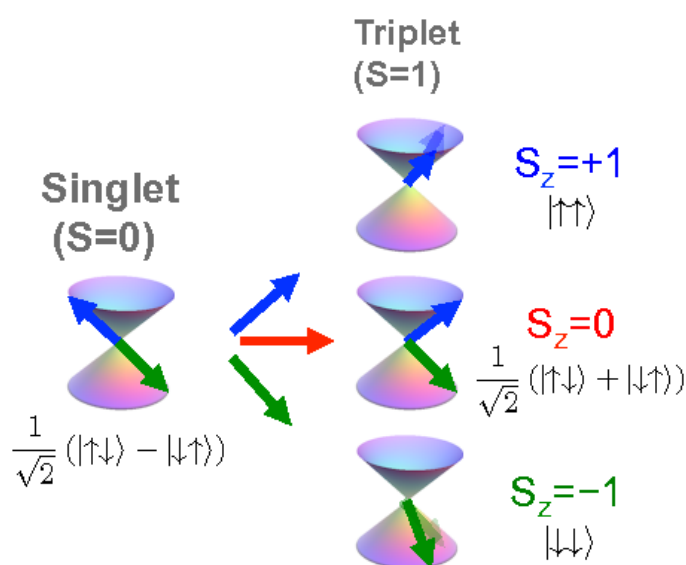
Figure 2.3.1 Spin statistics of a 2-electron system where the first spin wavefunction has $S = 0$ and m=1. The other three spin wavefunctions have $S = 1$ and $m = 3$. They only differ in the z-component of the spin, which can take one of three eigenvalues ($S_z = 1, 0, -1$).

2.4 Frank-Condon principle
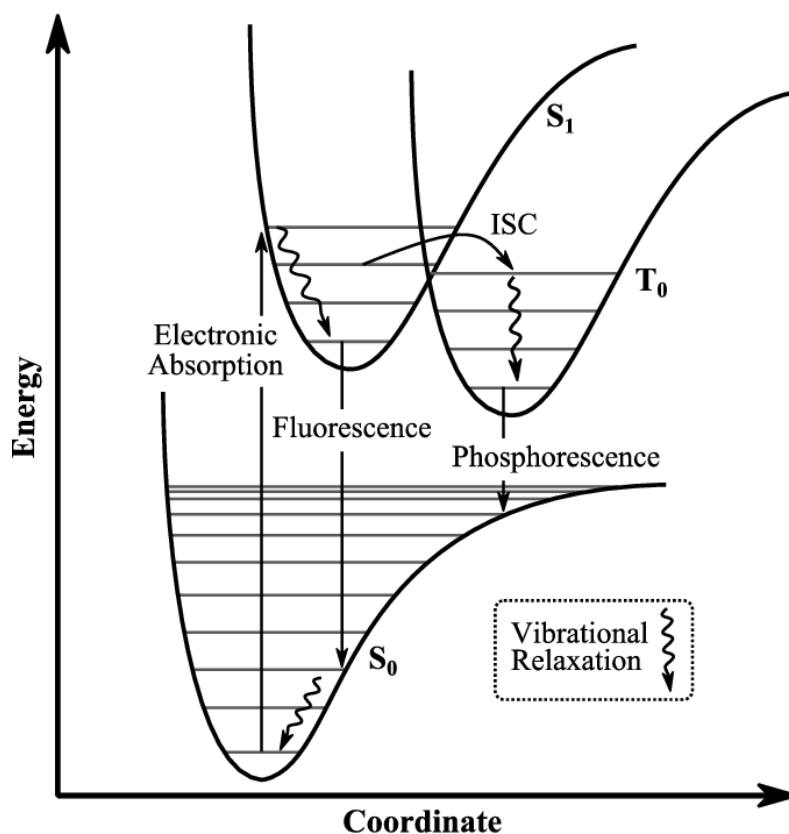
Figure 2.4.1 Potential energy diagrams with vertical transitions (Franck–Condon principle).

The Franck–Condon principle is a rule in spectroscopy and quantum chemistry that explains the intensity of vibronic transitions. The basis of the Franck–Condon principle is that an electronic transition is most likely to occur without changes in the positions of the nuclei in the molecular entity and its environment. The resulting state is called a Franck–Condon state, and the transition is called vertical transition. At room temperature, the molecule starts out in the $v = 0$ vibrational level of the ground electronic state and upon absorbing a photon with the necessary energy, makes a transition to the excited electronic state. The electron configuration of the new state may result in a shift of the equilibrium position of the nuclei constituting the molecule as shown in figure 2.4.1. In the electronic excited state molecules quickly relax to the lowest vibrational level of the lowest electronic excitation state via vibrational relaxation as shown in figure 2.4.1 and in the Jablonski diagram of figure 2.4.2, and from there it can decay to the electronic ground state via photon emission. The width of a band in the absorption spectrum is a result of two effects: the homogeneous (Lorentzian-shaped) and inhomogeneous broadening. The homogeneous broadening is due to the existence of a continuous set of vibrational sublevels

in each electronic state. The inhomogeneous (Gaussian) broadening results from the fluctuations of the structure of the solvation shell surrounding the chromophore[21].
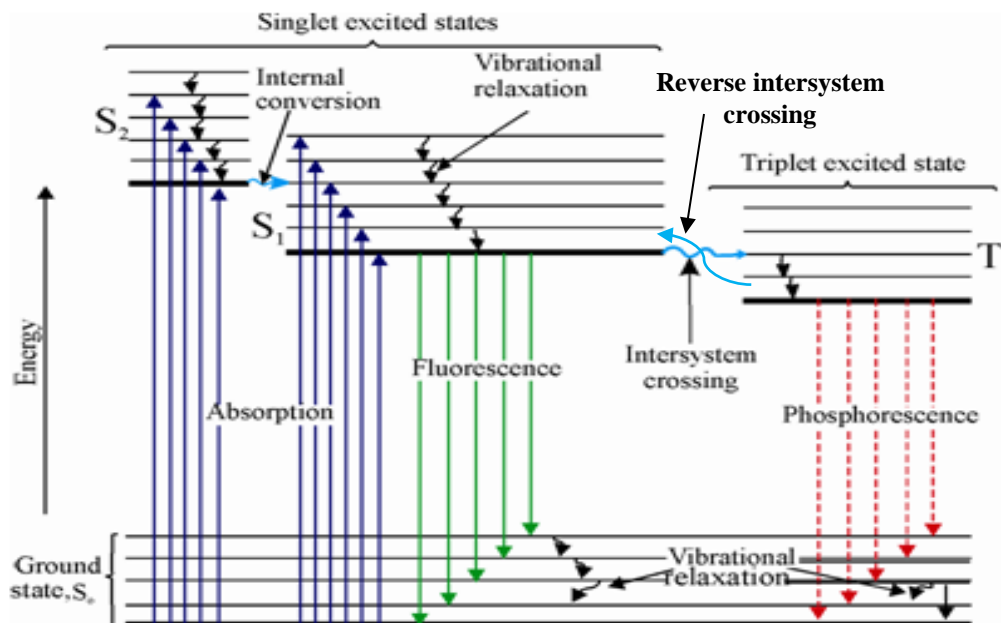
Figure 2.4.2 Jablonski diagram of the energy levels within a molecule showing valence excitations.

2.5 Transition between electronic states

In the electronic transitions of TADF-based OLEDs, the selection rules will provide the probability of a transition. The selection rules between electronic states can be related to the oscillator strength (f), which is a dimensionless quantity, expresses the probability of absorption or emission of electromagnetic radiation.

2.5.1 The parity

The Laporte rule states that the initial and final wavefunctions must be different to conserve parity, either symmetry or antisymmetry with respect to an inversion center. For example, g → g or u→ u is forbidden. Allowed transitions must involve a change in parity, either g → u or u → g. Also, the transition $\pi \to \pi^*$ is allowed, as the bonding (π) and anti-bonding (π^*) orbitals do not have the same parity.

2.5.2 The spin

The spin rule between two states need to be the same ($\Delta S = 0$). The optical transitions with change in the spin multiplicity such as phosphorescence (PH) are forbidden, however this rule is broken by spin-orbit coupling (SOC).

2.5.3 Orbital symmetry

The two orbitals involved in a transition must possess large amplitudes in the same region, otherwise the transitions are "overlap forbidden". For example, a $\pi \to \pi^*$ transition is allowed as their orbital lie in the same plane and have a high degree of spatial overlap. On the other hand, a $n \to \pi^*$ transition is forbidden.

2.6 Intersystem Crossing and Reverse Intersystem Crossing

In OLEDs, the T_1 state usually lies below the S_1 state, a statement which is strictly true is absence of medium and solvent effects, i.e. in gas phase. The process to convert a singlet excited state to a triplet excite state is termed InterSystem Crossing (ISC). The probability of this process to occur is more favorable when the vibrational levels of two excited states overlap, since little or no energy must be gained or lost in the transition. ISC is a non-radiative, diabatic process that occurs between states of different multiplicity. ISC for S_1 can occur either from zero-point vibrational level of S_1 or from thermally populated higher vibrational level of S_1 (the latter situation is referred to as "hot exciton"). The electron is transferred to the triplet excited states close in energy, either in T_1 or T_n. Being transitions between states of different spin multiplicity forbidden, they become partially allowed only if there is a substantial spin-orbit coupling (SOC) between the states[22].

The inverse process, namely the transformation of a triplet excited state into a singlet excited state, is not surprisingly called Reverse InterSystem Crossing (RISC) as shown in figure 2.4.2, and plays an important role in the TADF mechanism. As the S_1 state lies higher than the T_1 state, the energy difference ΔE_{ST} must be small to be overcome via the thermal energy[23]. Thus, ΔE_{ST} acts as the activation energy, or part of it (see below), for RISC to occur.

2.7 Origin of Singlet and triplet energy splitting

The energy splitting ΔE_{ST} is a fundamental parameter in governing the Thermally Activated Delayed Fluorescence process. Three energy terms are considered to calculate the energy of the lowest excited state: the orbital energy (E_{orb}), the electron repulsion energy (K) and the exchange energy (J). The orbital energy (E_{orb}) term describes the energy associated with the one-electron orbital in excited state, whereas the first order Coulombic correction is expressed by the electron repulsion energy (K) term. The exchange energy (J) term describes the first order quantum-mechanical correction involving electron-electron repulsion due to the Pauli principle, for two electron residing in the same region of space[13]. Therefore, the singlet and triplet states energies are given in equation 2.7.1 and 2.7.2 respectively. Due to the different spin of singlet and triplet excited states, the exchange energy term increases the energy in S_1 state and decrease in T_1 state by the same amount.

$$E_{S1} = E_{orb} + K + J \qquad (2.7.1)$$

$$E_{T1} = E_{orb} + K - J \qquad (2.7.2)$$

$$\Delta E_{ST} = E_{S1} - E_{T1} = 2J \qquad (2.7.3)$$

According to equation 2.7.1 and 2.7.2, the singlet-triplet energy gap is given by 2.7.3. Therefore, ΔE_{ST} depends on the exchange energy, which is proportional to the excited state and ground state wavefunctions overlap.

$$J = \iint \phi(r_1)\psi(r_2)(\frac{e^2}{r_1 - r_2})\phi(r_2)\psi(r_1)dr_1 dr_2 \qquad (2.7.4)$$

where ϕ and ψ are defined as the wavefunctions of HOMO and LUMO respectively, and e is the electron charge.

To a first order approximation, the exchange interaction scales exponentially with the overlap of the respective electron wavefunctions. If the wavefunctions of the electron in the HOMO and that in the LUMO overlap significantly($\phi(r_1)\psi(r_2) \neq 0$ in some regions of the molecules), a large exchange energy $2J$ in the order of 0.7-1.0 eV will result. Smaller exchange energies, in the range of $0.2 - 0.5$ eV, occur in molecules where HOMO and LUMO are located on different

parts of the molecules, or in other words where the $S_0 \rightarrow S_1$ and $S_0 \rightarrow T_1$ transitions have at least a partial CT character.

2.8 Spin orbit coupling

As discussed later in this chapter, the rate of RISC plays crucial role in the TADF process. Within the Condon approximation, the k_{RISC} between one singlet and one triplet state can be described in equation 2.8.1 using Fermi's golden rule without the coupling between electronic and vibrational motion.

$$k_{RISC} \propto |\langle \psi_T | \hat{\mathcal{H}}_{SOC} | \psi_S \rangle|^2 \sum_{k,j} |\langle v_{Tk} | v_{Sj} \rangle|^2 \qquad (2.8.1)$$

where v are the vibrational energy level and $\hat{\mathcal{H}}_{SOC}$ is the spin-orbit Hamiltonian. The δ is the function that ensures the conservation of the molecular energy for a nonradiative transition. It is clear to see that, without taking into account for the vibrational motions, the RISC rate is driven by spin-orbit coupling[24]. The SOC is a relativistic interaction of a particle spin with its motion inside a potential, leading to shifts in the electronic energy levels due to the electromagnetic interaction between the electron is magnetic dipole, its orbital motion, and the electrostatic field of the positively charged atomic nucleus. In the high-temperature regime, the Franck-Condon weighted density of states $\sum_{k,j} |\langle v_{Tk} | v_{Sj} \rangle|^2$ obeys a standard Arrhenius-type equation, and the rate takes the classical expression:

$$k_{RISC} = A \cdot \exp(-\frac{\Delta E_{ST}}{kT}) \qquad (2.8.2)$$

where k is Boltzmann constant, T is the temperature, and the prefactor A is proportional to the squared SOC electronic coupling $V_{SOC}^2 = |\langle \psi_T | \hat{\mathcal{H}}_{SOC} | \psi_S \rangle|^2$. If one instead consider the coupling with one effective classical vibrational mode, the RISC rate can be expressed, within semi-classical Marcus theory, as[25]:

$$k_{rISC} = \frac{2\pi}{\hbar} V_{SOC}^2 \frac{1}{\sqrt{4\pi\lambda kT}} \exp\left[-\frac{(\lambda+\Delta E_{ST})^2}{4\lambda kT}\right] \qquad (2.8.3)$$

where the reorganization energy $\lambda = \lambda_{out} + \lambda_{in}$ contains (classical) contributions of low-frequency modes for the surrounding medium λ_{out} and intramolecular high-frequency vibrational modes λ_{in}.

One effective strategy to increase the spin orbit coupling (SOC) is the so-called heavy-atom effect, i.e. the insertion of heavy (transition metal) atoms in the organic framework, efficiently exploited in the popular phosphorescent iridium-based emitters[22]. However, organic material consists of hydrogen and carbon atoms and thus tend to have weaker spin-orbit coupling, which means that the spin-flip mechanism of ISC and RISC is not efficient. For TADF-based OLEDs, V_{SOC} is enhanced by including the heavy metal, and a strong mixing of spin orbitals of S and T excited state is induced. Alternatively, to drive such efficient ISC and RISC without heavy metal atoms, a small ΔE_{ST} will increase the value of a first-order mixing coefficient (γ) between singlet and triplet excited state[26,27].

$$\gamma \propto \frac{V_{SOC}}{\Delta E_{ST}} \qquad (2.8.4)$$

It follows from equation 2.8.4 that heavy atoms are not required to achieve efficient spin conversion when a molecule possesses a small ΔE_{ST} and V_{SOC} is not vanishingly small.

2.9 Internal quantum efficiency in presence of Delayed Fluorescence

Delayed fluorescence occurs when a molecule in the T_1 state goes through a transition to the S_1 state followed by a radiative transition to S_0, which results in an emission identical in wavelength to prompt fluorescence, but occurring on a longer timescale. Delayed fluorescence occurs through two distinct mechanisms: thermally activated delayed fluorescence (known as E-type[21]) and triplet-triplet annihilation (known as P-type). In this context, only the details about TADF will be given.
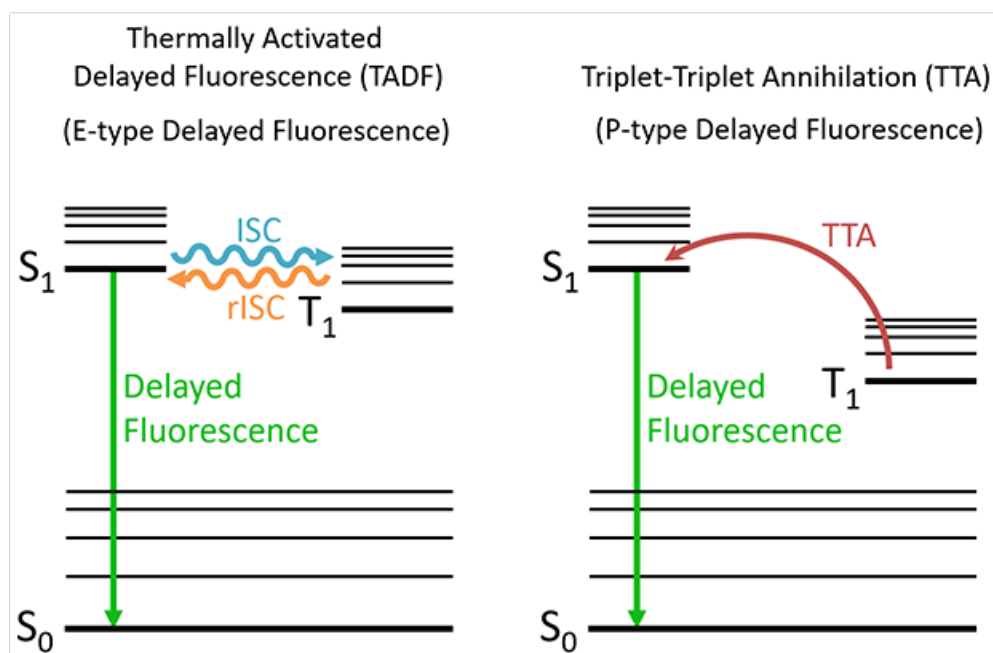
Figure 2.9.1 Mechanism of delayed fluorescence: Thermally Activated Delayed Fluorescence (left) and Triplet-Triplet Annihilation (right)

Thermally activated delayed fluorescence (TADF) is the process when the molecule transitions from the T_1 state back into the S_1 state through reverse intersystem crossing (RISC). Because of the small energy gap between first singlet and first triplet state, the excitons at T_1 state are able to thermally access to S_1 state, leading the transition from S_1 to S_0 to be delayed fluorescent. Recent studies of TADF based-OLED have achieved an internal quantum efficiency of nearly 100 %. The performance of TADF emitter depends on the rate of RISC which for simplicity here we describe with equation 2.9.1. In TADF-based OLEDs, internal quantum efficiency (IQE), i.e. the ratio between emitted photons and produced excitons, is therefore arising from several electronic processes: prompt fluorescence (PF), delayed fluorescence (DF), and direct and reverse intersystem crossing (ISC, RISC)[12]. To achieve high efficiency, the photoluminescence quantum yield (PLQY) of PF ($\emptyset_{PF}$) and of DF ($\emptyset_{DF}$) should be maximized as suggested by the following equation:

$$\eta_{int} = n_{r,S}\emptyset_{PF} + n_{r,S}\emptyset_{DF} + n_{r,T}\frac{\emptyset_{DF}}{\emptyset_{ISC}} \qquad (2.9.1)$$

where η_{int} is the internal quantum efficiency (IQE), $n_{r,S}$ is the singlet exciton generation efficiency (0.25), $n_{r,T}$ is the triplet exciton production (0.75), $\emptyset_{ISC}$ is the quantum yield of singlet to triplet intersystem crossing (inversely proportional to the RISC one). Obviously, high IQE in TADF based-OLEDs emitters can be reached with high $\emptyset_{PF}$, high $\emptyset_{DF}$ and low $\emptyset_{ISC}$

values. The $\emptyset_{PF}$ can be enhanced by efficient fluorescence process while $\emptyset_{DF}/\emptyset_{ISC}$ can be maximized by minizing the singlet-triplet energy gap splitting as shown in equation 2.9.2.

$$\frac{\emptyset_{DF}}{\emptyset_{ISC}} = \frac{1}{1+\dfrac{k_{nr}}{\emptyset_{PF}A\exp(-\dfrac{\Delta E_{ST}}{kT})}} \qquad (2.9.2)$$

2.10 Summary of experimental results for 2CzBN and 4CzBN

The experimental work from Adachi and co-workers shows that 2CzBN and 4CzBN have a $\Delta E_{ST} \sim 0.2$ eV which is a slightly large to achieve efficiency RISC at room temperature. However, 4CzBN shows a high external quantum efficiency (EQE) $\sim$ 20 %, while 2CzBN is a TADF-inactive emitter. However, all the molecules are TADF-inactive in presence of O_2 in toluene as the result shows in figure 10.1.1.
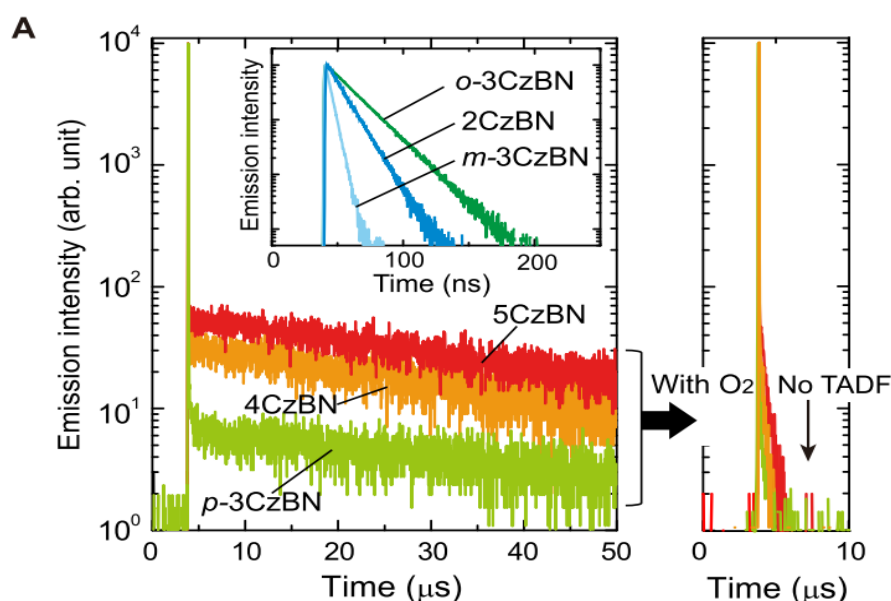
Figure 10.1.1 Photoluminescence decay curve of CzBN derivatives in toluene at 298K where 2CzBN shows only prompt fluorescence while 4CzBN shows both prompt fluorescence and delayed fluorescence. Figure adapted from reference 18.

These data implied that, to achieve high rate of RISC, a $\Delta E_{ST} \sim 0.2$ eV does not play an important role. They clarified that the formation of a delocalized CT state is the key to promote a large k_{RISC} even when the energy-splitting of S_1 and T_1 is not close to zero. They also pointed

out the restriction of structure relaxation in the T_1 state to achieve a high PLQY. Linearly positioning of carbazole pair connected with respect to the benzonitrile unit may cause the structure relax, depending on the free space around it, to deactivate the T_1 state. As a result, they propose the structure to form delocalized CT by keeping it rigid, i.e. by introducing bulky moieties around the donor unit in a D-A-D structure.
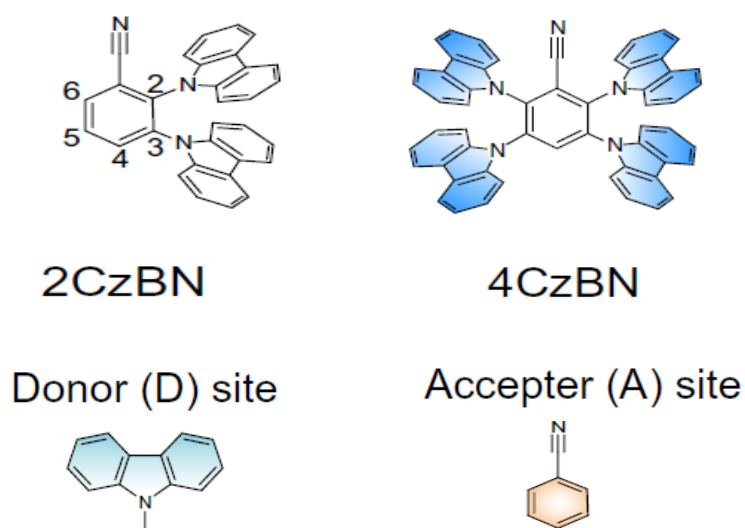
Figure 10.1.2 Molecular structure of 2,3-di(9*H*-carbazol-9-yl)benzonitrile (2CzBN) and 2,3,5,6-tetra(9*H*-carbazol-9-yl)benzonitrile (4CzBN) where carbazole is a donor group and benzonitrile an acceptor group. Figure adapted from reference 18.

Chapter 3

Electronic structure of 2CzBN and 4CzBN

Two molecules, namely 2,3-di(9*H*-carbazol-9-yl)benzonitrile (2CzBN), which is inactive as TADF emitter, and 2,3,5,6-tetra(9*H*-carbazol-9-yl)benzonitrile (4CzBN), which exhibits TADF[18], were selected to characterize their ground excited state properties, looking for a deeper understanding of the effect of their donor-acceptor (D-A) and donor-acceptor-donor (D-A-D) structures, on the efficiency of reverse intersystem crossing (RISC). As mentioned in Chapter 2, Carbazole (Cz) plays the role of electron donating (D) group, while benzonitrile (BN) is the electron accepting (A) group. In this section we compare the potential energy surfaces of the two molecular architectures, also as a function of Cz-BN dihedral angles, with a combination of DFT calculations for the ground state and TD-DFT calculations for excited state.

3.1 Geometry optimization of 2CzBN and 4CzBN
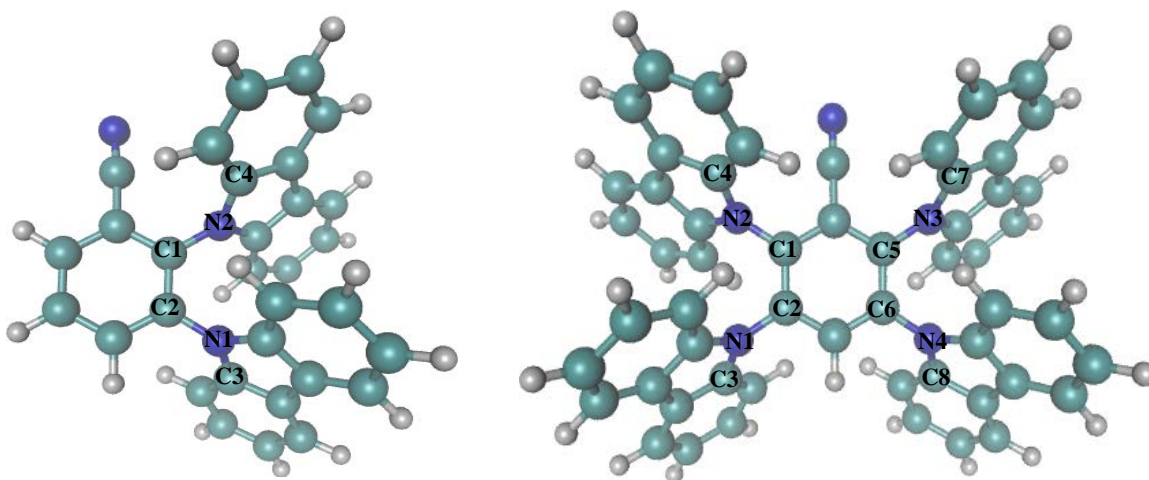
Figure 3.1.1 The PBE0/6-31G* optimized structure of 2CzBN (left) and 4CzBN (right) where Cz-BN dihedral angles are defined as $\varphi_1 = C_1-C_2-N_1-C_3$ and $\varphi_2 = C_2-C_1-N_2-C_4$ for 2CzBN and as $\varphi_1 = C_2-C_1-N_2-C_4$, $\varphi_2 = C_1-C_2-N_1-C_3$, $\varphi_3 = C_6-C_5-N_3-C_7$ and $\varphi_4 = C_5-C_6-N_4-C_8$ for 4CzBN.

The geometrical and electronic properties of 2CzBN and 4CzBN were first obtained with the Gaussian 09 program package. The ground state (S_0) of 2CzBN was first optimized by means of DFT calculations with the PBE0 hybrid functional with the moderate basis set 6-31G*[11], then the calculation was improved with the cc-pVTZ basis set. The optimized structures

were used to compute the vibrational frequencies in order to check the structural stability[28]. No imaginary frequencies are found as expected for a geometry corresponding to an absolute minimum of the PES. The optimized structures of 2CzBN and 4CzBN are shown in figure 3.1.1, where the carbazole-benzonitrile dihedral angles used in the potential energies scan described in the following are also defined. The calculated equilibrium values of dihedral angles were $\varphi_2 = -123.1°$ and $\varphi_2 = -118.4°$ for 2CzBN, and $\varphi_1 = 119.5°$, $\varphi_2 = 124.5°$, $\varphi_3 = -119.7°$ and $\varphi_4 = -124.5°$ for 4CzBN. Due to the molecular symmetry of 2CzBN we expected at least four minima points in the whole scan from -180° to 180°, at ± 60° and at ± 120°. We found that also for 4CzBN structures with φ_1 and φ_2 equal to ± 60° are nearly equivalent in energy to the structures with φ_1 and φ_2 equal to ± 120°. All the gas phase optimization results are given in table 3.1.

Table 3.1 Calculated ground state (S_0) energy (hartree) and dihedral angles (deg) of 2CzBN and 4CzBN at the optimized geometry.

Molecule	Functional/basis set	φ_1	φ_2	φ_3	φ_4	Optimized energy
2CzBN	PBE0/6-31G*	-123.1	-118.4	-	-	-1355.45834
		-60	-60	-	-	-1355.45829
		-120	-120	-	-	-1355.45824
	PBE0/cc-pVTZ	-122.8	-118.0	-	-	-1355.86965
4CzBN	PBE0/6-31G*	119.5	124.5	-119.7	-124.5	-2386.81026
		60	60	-115.5	-121.9	-2386.81018
		120	120	-120.2	-125.1	-2386.81023

In table 3.1, we also report the geometries with both dihedral angles fixed to -60° and -120° (or 60° and 120° if dihedral angle was defined with positive value) which also confirmed to be minima of the PES during the torsional energy profile scan. During the geometry optimization one can reach one of the two minima depending on the initial geometry. Interestingly, for 4CzBN, when φ_1 and φ_2 are fixed to 60° and 120° while letting the φ_3 and φ_4 relax, the values of φ_3 and φ_4 do not change much. Therefore, for simplicity we will only compute the potential energy scan of 4CzBN with respect to only 2 dihedral angles (either φ_1 and φ_2, or the φ_3 and φ_4 letting the other two at their equilibrium values). We assume that the variation of the other two dihedrals would bring the same, additive variation of any electronic property.

3.2 Frontier orbitals characterization

We then investigated the shape and energy of frontier molecular orbitals at the equilibrium geometry. Figure 3.2.1 shows that for 2CzBN, HOMO is localized on carbazole group while LUMO is localized on benzonitrile. For 4CzBN, LUMO is also localized on benzonitrile group but HOMO is localized on the whole region of 4CzBN molecule. As expected, carbazole moieties appear to be the donor group, while benzonitrile behave as acceptor group: 2CzBN and 4CzBN actually correspond to D-A and D-A-D architecture. The energy separation between HOMO and LUMO of 2CzBN and 4CzBN are 4.170 eV and 3.805 eV, respectively. This suggests that 2CzBN should possess a slightly larger band gap than 4CzBN, consequently 2CzBN absorption/emission is bluer than that of 4CzBN. This result is in agreement with experimental result which shows 2CzBN absorption is blue-shifted with respect to 4CzBN[18]. We also note that both 2CzBN and 4CzBN have frontier orbitals close in energy to HOMO (HOMO-1 as shown in figure 3.2.2).

HOMO

(-5.811 eV)

LUMO

(-1.685 eV)

HOMO

(-5.776 eV)

LUMO

(-1.942 eV)
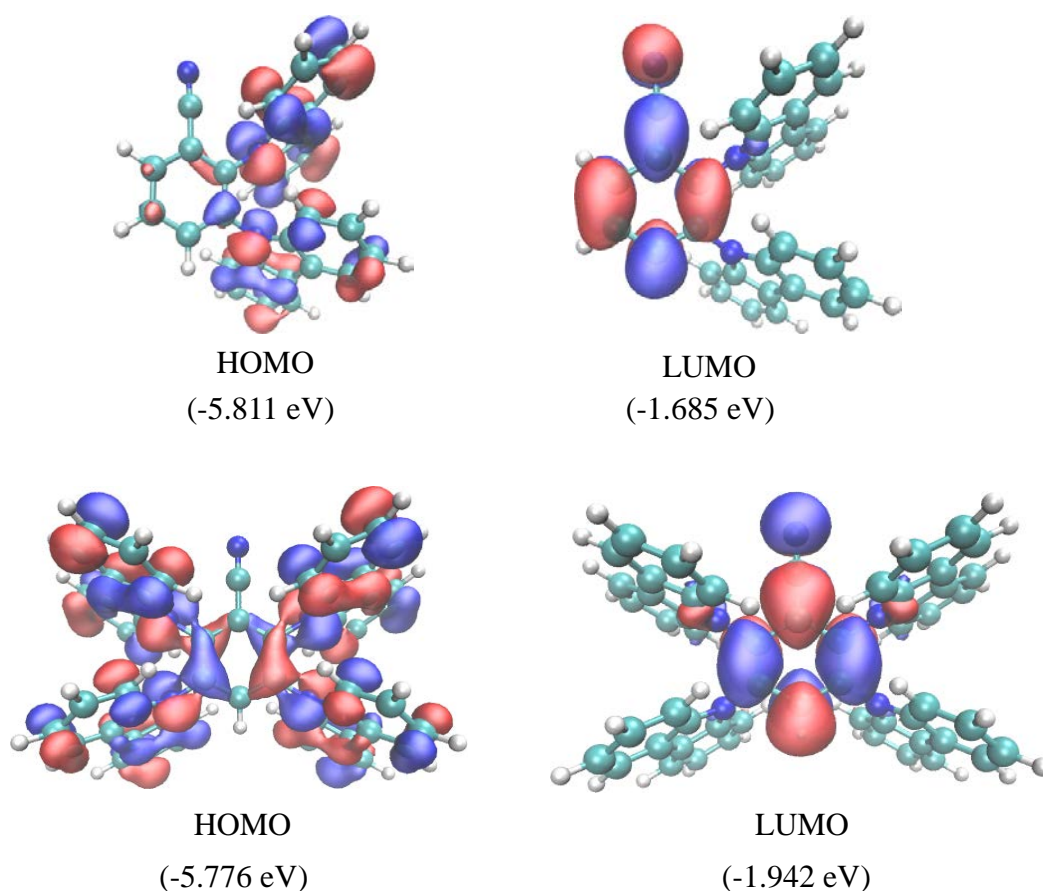
Figure 3.2.1 Isocontour plots (cutoff=0.02 a.u.) of frontier orbitals (HOMO and LUMO) of 2CzBN (top) and 4CzBN (bottom) calculated at the PBE0/6-31G* (at the equilibrium geometry)

HOMO-1
(-5.912 eV)

LUMO+1
(-1.096 eV)

HOMO-1
(-5.961 eV)
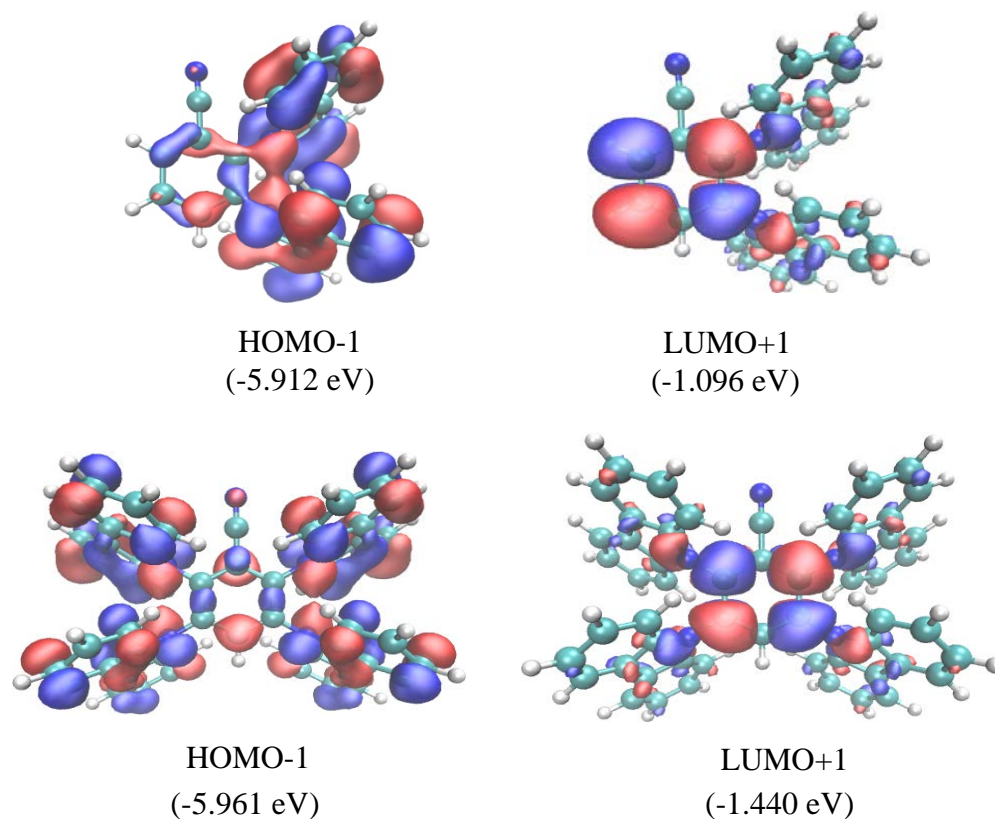
LUMO+1
(-1.440 eV)

Figure 3.2.2 Isocontour plots (cutoff = 0.02 a.u.) of frontier orbitals (HOMO-1 and LUMO+1) of 2CzBN (top) and 4CzBN (bottom) calculated at the PBE0/6-31G* (at the equilibrium geometry)

The difference in energy of HOMO and HOMO-1 of 2CzBN and 4CzBN are 0.098 eV and 0.196 eV respectively. The HOMO and HOMO-1 orbital shape 4CzBN are very similar, while for 2CzBN HOMO-1 is still similar but more delocalized into the benzonitrile ring. In the table 3.2 are given all the frontier orbitals that are relatively close in energy to HOMO and LUMO, calculated not only in gas phase but also in toluene with the polarizable continuum model (PCM). Toluene appears to stabilize all the orbital energies without altering the general trend.

Table 3.2 Frontier molecular orbital energies of 2CzBN and 4CzBN as obtained with the level of calculation PBE0//6-31G* in gas phase and with implicit solvation model for toluene (PCM model, $\varepsilon = 2.3741$))

Molecular orbital	Orbital Energy (eV)			
	2CzBN		4CzBN	
	Gas phase	PCM	Gas phase	PCM
HOMO-2	-6.064	-6.141	-6.038	-6.100
HOMO-1	-5.912	-5.964	-5.961	-6.019
HOMO	-5.811	-5.866	-5.766	-5.823
LUMO	-1.685	-1.696	-1.942	-2.018
LUMO+1	-1.096	-1.063	-1.440	-1.481
LUMO+2	-0.729	-0.764	-0.822	-0.856

3.3 Excited state calculation of 2CzBN and 4CzBN

The excited states were then calculated using time-dependent density functional theory (TD-DFT) calculations with PBE0/6-31G* and then improving the calculation accuracy with the larger cc-pVTZ basis set. The excited energies of triplet and singlet were calculated based on the optimized ground states geometry[29]. The vertical excitation energy was computed for absorption from the ground state S_0 to the first singlet S_1 ($E_V(S_1)$) and triplet T_1 ($E_V(T_1)$) excited-states; the calculation yields correspondingly the vertical singlet–triplet gap as $\Delta E^{ST} = E_V(S_1) - E_V(T_1)$. Since, Adachi and co-workers conducted experiments in toluene for these compounds, the solvent effects was again included by using the non-equilibrium Polarizable Continuum Model for excited state calculations[11]. The state energies and the calculated vertical gap ΔE^{ST} at the minimum energy conformer of 2CzBN and 4CzBN in the presence of toluene ($\varepsilon = 2.3741$) are compared with the experimental values from Adachi and co-workers[18]. Oscillator strength (O.S.) are also given in tables 3.3.1 and 3.3.2. For 2CzBN results show that the use of cc-pVTZ basis set gave the energy of vertical singlet–triplet gap slightly closer to experimental value than the use of 6-31G* basis set, even if the two gaps are very similar. More importantly, the vertical energy splitting of singlet and triplet in both compounds are approximately the same (0.28-0.30 eV), which are rather high to drive an efficient performance; however despite the nearly equal ΔE^{ST} the TADF performance of the two compounds is completely different. Therefore, the key to drive the rate of RISC in 2CzBN and 4CzBN should

not depends on ΔE^{ST}, but on other parameters such as the oscillator strength. Indeed, both basis sets gave rather low values for 2CzBN oscillator strength, and larger ones for 4CzBN, indicating a more efficient light emission for the latter compound. The problem of small oscillator strength from S_1 to S_0, which eventually leads to low photoluminescence quantum efficiency in TADF based-OLEDs, will be addressed further in this chapter. The comparison between gas phase and solvent calculation, shows values closer to experimental results and higher oscillator strengths in the presence of toluene, both for 2CzBN and 4CzBN.

Table 3.3.1 Calculated vertical transition energies, singlet-triplet energy gaps, and oscillator strengths (O.S) at the equilibrium geometry of 2CzBN, calculated in gas phase and in toluene (PCM model, $\varepsilon = 2.3741$). Experimental values from reference 18 are given between round brackets. [a]Note that the oscillator strength is only defined for singlet excitation.

Functional/basis set	States	Energy (eV)		O.S[a]	
		PCM model*	Gas phase	PCM model*	Gas phase
PBE0/6-31G*	S_1	3.313	3.283	0.0429	0.0306
	S_2	3.436	3.416	0.0002	0.0005
	T_1	3.004	2.972	-	-
	T_2	3.079	3.071	-	-
	ΔE^{ST}	0.309 (0.21)	0.311	-	-
PBE0/cc-pVTZ	S_1	3.319	-	0.0401	-
	S_2	3.436	-	0.0003	-
	T_1	3.035	-	-	-
	T_2	3.089	-	-	-
	ΔE^{ST}	0.283 (0.21)	-	-	-

Table 3.3.2 Calculated vertical transition energies, singlet-triplet energy gaps, and oscillator strengths (O.S) at the equilibrium geometry of 4CzBN, calculated in gas phase and in toluene (PCM model, $\varepsilon = 2.3741$). Experimental values from reference 18 are given between round brackets. [a]Note that the oscillator strength is only defined for singlet excitation.

Functional/basis set	States	Energy (eV)		O.S[a]	
		PCM model*	Gas phase	PCM model*	Gas phase
PBE0/6-31G*	S_1	2.963	2.993	0.1364	0.1061
	S_2	3.157	3.156	0.0101	0.0088
	T_1	2.7402	2.736	-	-
	T_2	2.7845	2.800	-	-
	ΔE^{ST}	0.223 (0.22)	0.257	-	-

We also computed the absorption spectrum of 2CzBN and 4CzBN by using time-dependent density functional theory (TD-DFT) with PBE0/6-31G* and PCM for toluene. The calculation shows that the spectrum of 4CzBN is strongly red-shifted respect to 2CzBN. The D-A-D structure shows a more red-shifted spectrum than the D-A one (in figure 3.3.1). This result is corresponding to the different HOMO-LUMO gap in table 3.2 as the energy gap of 2CzBN is larger than 4CzBN and it is also in agreement with experimental result from Adachi and co-worker[18].
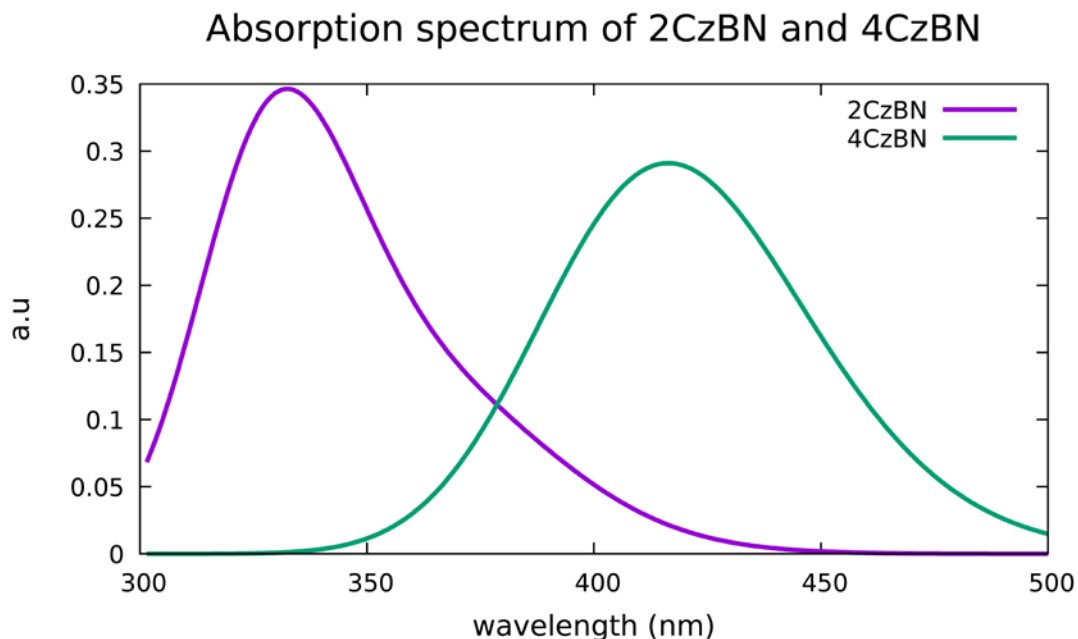
Figure 3.3.1 The absorption spectrum of 2CzBN and 4CzBN calculated by using TD-PBE0/6-31G* with PCM model (Gaussian function: broadening 0.2 eV).

The influence of molecular geometry and the interaction with the solvent provides a possible source variability in the excitation energy, leading to broadening in the transition from S_1 to S_0 as shown in figure 3.3.1, where a Gaussian broadening of 0.2 eV was applied to the TDDFT energies. However, this broadening partially hides that the spectral features arise from the presence of low-lying singlets excited states close in energy levels. The electronic transitions that are involved in the spectrum of 2CzBN and 4CzBN are more neatly shown in figure 3.3.2., where a narrow Gaussian broadening was applied. The orbitals contributing to spectrum for each transition of 2CzBN and 4CzBN with no vanishing oscillator strength are given in table 3.3.3:
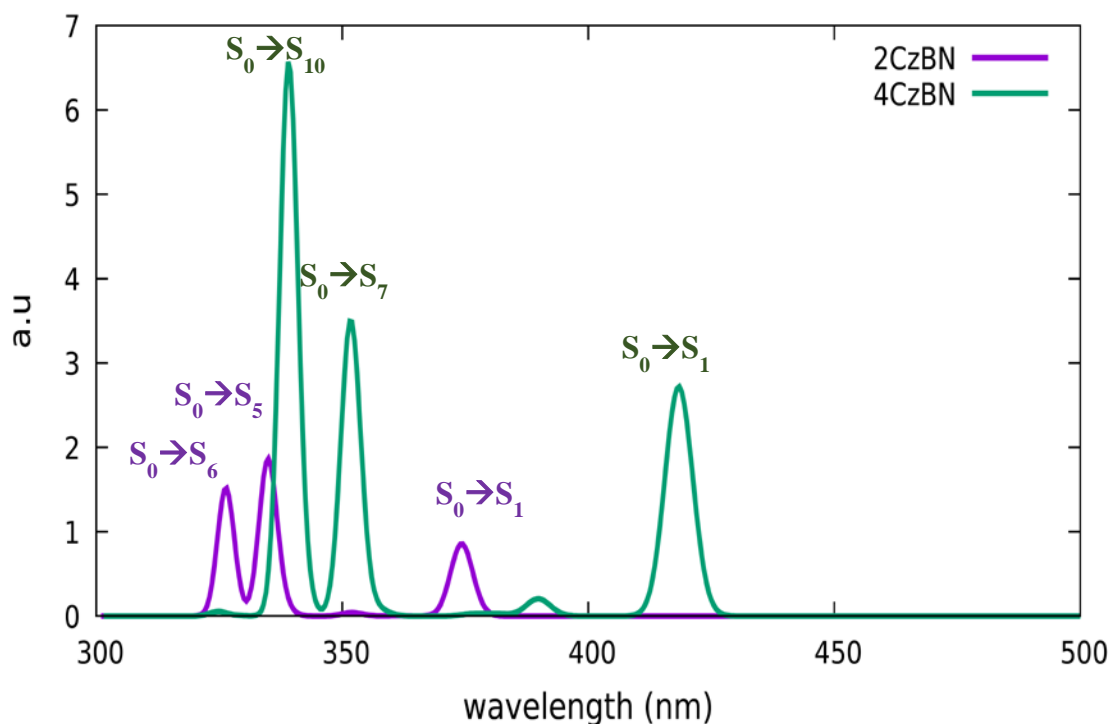
Figure 3.3.2 The absorption spectrum of 2CzBN and 4CzBN calculated by using TD-PBE0/6-31G* with PCM model (Gaussian function: broadening 0.02 eV).

The frontier orbitals that mostly contribute to the transition are HOMO-1, HOMO, LUMO and LUMO+1 in 2CzBN and 4CzBN. The transition from S_0 to S_{10} of 4CzBN has a high oscillator strength (0.3287) and corresponds to an excitation energy in the dark-blue region. We stress again that 4CzBN shows a higher oscillator strength than 2CzBN. This could be one of the reasons why 4CzBN is a TADF active emitter, while 2CzBN is not. Figure 3.3.3 we show instead the dependence on carbazole conformation of the $S_0 \rightarrow S_1$ excitation energy: the variability is larger for 2CzBN, and the lowest excitation energies are found at $\pm 90^o$, $\pm 90^o$, and not at the Franck-Condon points $\pm 60^o$, $\pm 60^o$ and $\pm 120^o$, $\pm 120^o$. 4CzBN shows similar features but less pronounced.

Table 3.3.3 Orbitals contributing to spectrum for each transitions of 2CzBN and 4CzBN, calculated in toluene (PCM model, ε = 2.3741). Excitation coefficients, excitation energy (nm) and oscillator strength are also given. Note the orbitals for 2CzBN (H=HOMO = 113 and L=LUMO =114) and for 4CzBN (H=HOMO = 199 and L=LUMO = 200).

	Transition	Orbital contribution	Coefficient of wavefunction	Excitation energy (nm)	Oscillator strength
2CzBN	$S_0 \rightarrow S_1$	H-1$\rightarrow$L H$\rightarrow$L	0.64092 0.28480	374.26	0.0429
	$S_0 \rightarrow S_5$	H-3$\rightarrow$L H$\rightarrow$L+1	-0.16703 0.67417	334.88	0.0924
	$S_0 \rightarrow S_6$	H-1$\rightarrow$L+1	0.69488	326.34	0.0762
4CzBN	$S_0 \rightarrow S_1$	H$\rightarrow$L	0.69580	418.39	0.1363
	$S_0 \rightarrow S_7$	H-1$\rightarrow$L H$\rightarrow$L+1	-0.11618 0.67735	351.72	0.1358
	$S_0 \rightarrow S_{10}$	H-1$\rightarrow$L+1	0.69809	339.10	0.3287
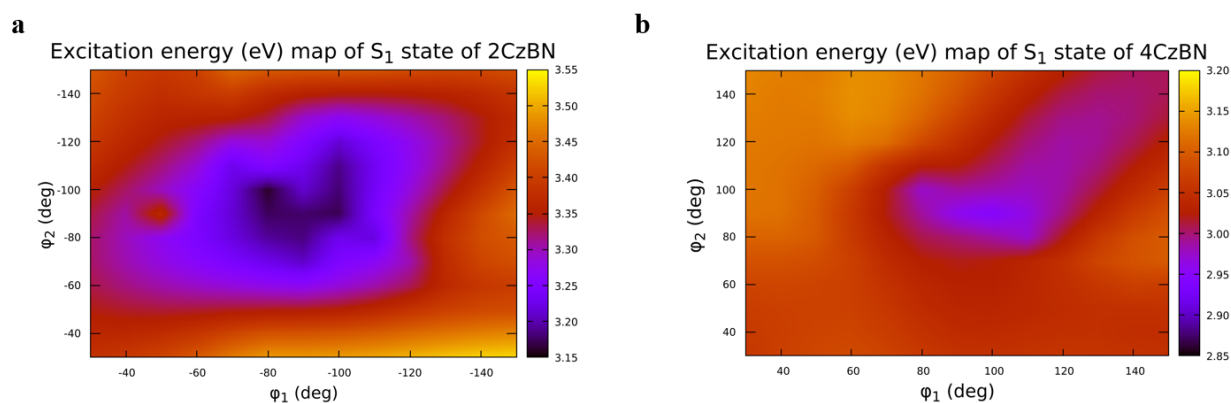
Figure 3.3.3 The vertical excitation energy from $S_0 \rightarrow S_1$ calculated by using TD-PBE0/6-31G* as a function of the two carbazole-benzonitrile dihedral angles for 2CzBN (plate a) and 4CzBN (plate b)

3.4 Torsional energy profiles of 2CzBN and 4CzBN

In order to investigate the possible conformations of the carbazole groups, the relaxed torsional energy profiles of two carbazole-benzonitrile dihedral angles were calculated. The potential energy surface of 2CzBN was explored by keeping fixed one dihedral angle (φ_1) while letting the other one relax (φ_2), and vice versa. The dihedral angle was scanned from 0° to -180° (only half of the range). The other half (from 0° to 180°) is leading to the same potential energy profile because of the symmetry of 2CzBN. The scan was calculated first at PBE0/6-31G* level. In figure 3.4.1, the torsional energy profiles of both scanning dihedral angles are similar. The two minima points are found at -120° and -60° while the saddle point is set at -90° with a difference in energy of ~3 kcal/mol. Actually, the profiles should exhibit mirror symmetry with respect to 90°, but they do not at the maxima, due to some hysteresis arising from the orientation of the second carbazole which does not change symmetrically during the optimization.
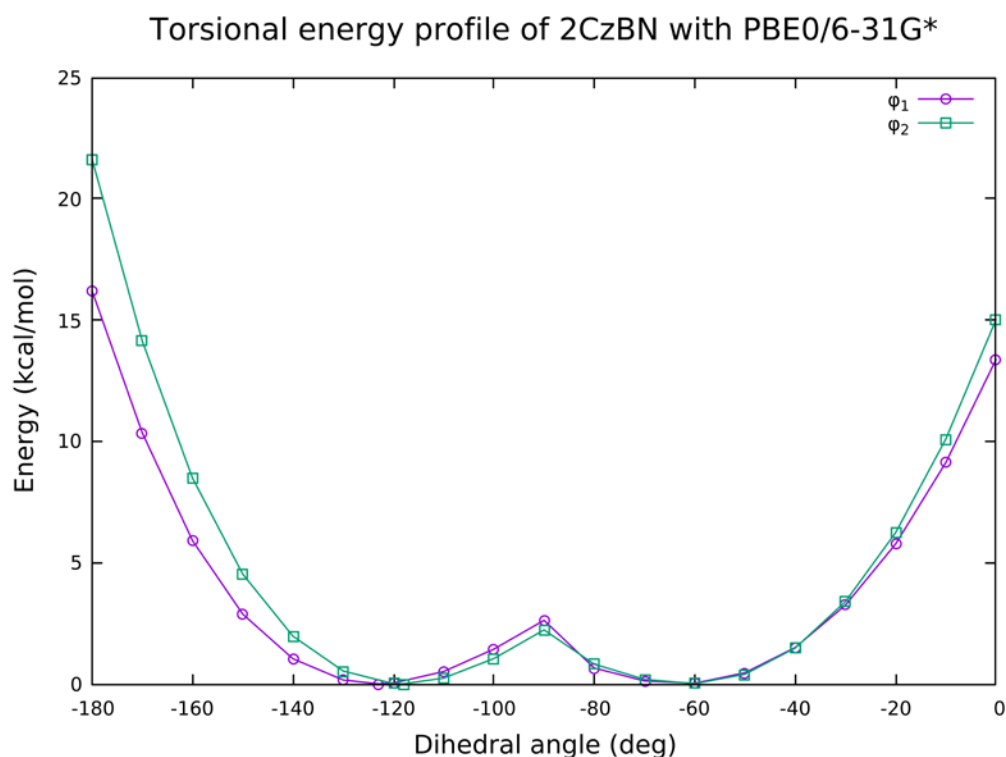
Figure 3.4.1 The potential energy surface relaxed scan of 2CzBN through the dihedral angles φ_1 and φ_2 with the level of calculation PBE0//6-31G*.

To improve the potential energy profile, the PES of 2CzBN was then obtained (single point calculation with respect to PBE0/6-31G* optimized conformations) with a bigger basis

set (cc-pVTZ, in figure 3.4.2). We have compared the basis sets 6-31G* and cc-pVTZ, observing that they lead to similar relative energies. The results are shown in figure 3.4.3. Then we opted for using the moderate basis set (6-31G*) to obtain the PES of 4CzBN, which is a bigger molecule and consequently more demanding in term of time and computational cost.
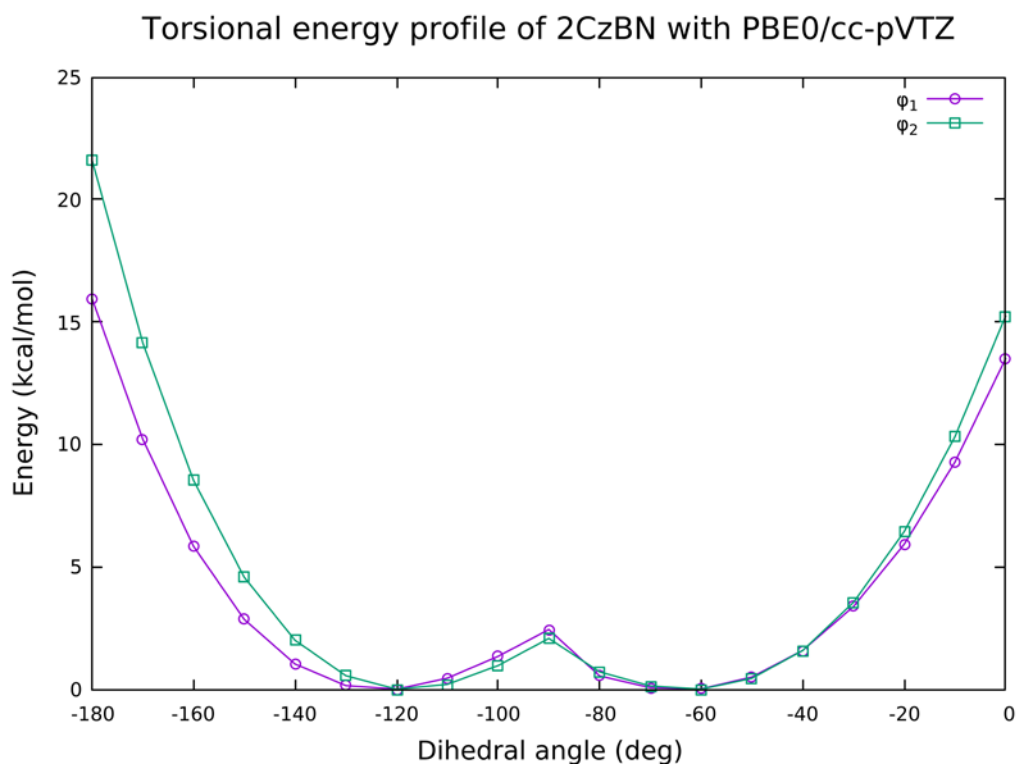
Figure 3.4.2 The single point calculation of potential energy surface scan of 2CzBN through the dihedral angles φ_1 and φ_2 with the level of calculation PBE0/6-31G*/cc-pVTZ.

The potential energy scan of each dihedral angle of 4CzBN was also computed with PBE0/6-31G* level. We only computed the PES of two dihedral angles scan which are φ_3 and φ_4, as the molecule is symmetric with respect to the plane perpendicular to the benzonitrile ring and passing through the CN bond. Also, in this case the dihedral angles were scanned from $0°$ to $-180°$ both φ_3 and φ_4. The profiles are shown in figure 3.4.4.
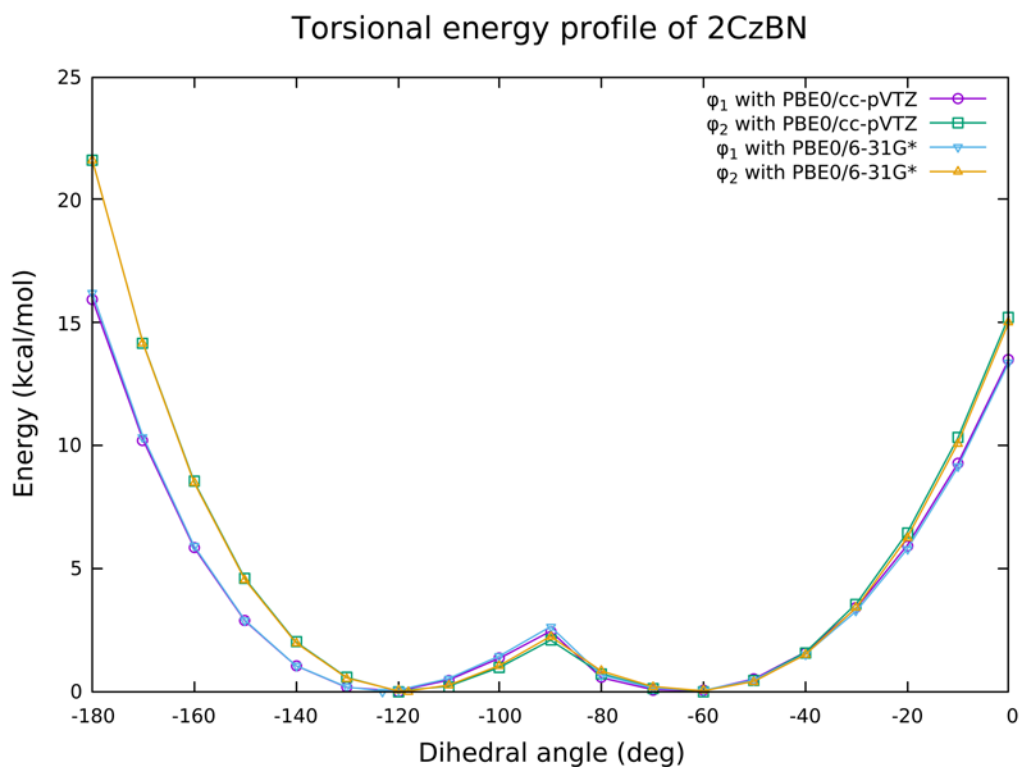
Figure 3.4.3 Comparison of torsional potential energy profile of 2CzBN through the dihedral angles φ_1 and φ_2 with the level of calculation PBE0/6-31G* and PBE0/6-31G*/cc-pVTZ.

The torsional energy profiles of both scanned dihedral angles of 4CzBN are similar. The two minima points are also found at -120° and -60° as for the 2CzBN. The saddle point is at the dihedral angle equal to -90° with a difference in energy with respect to the minima points of ~ 3 kcal/mol.
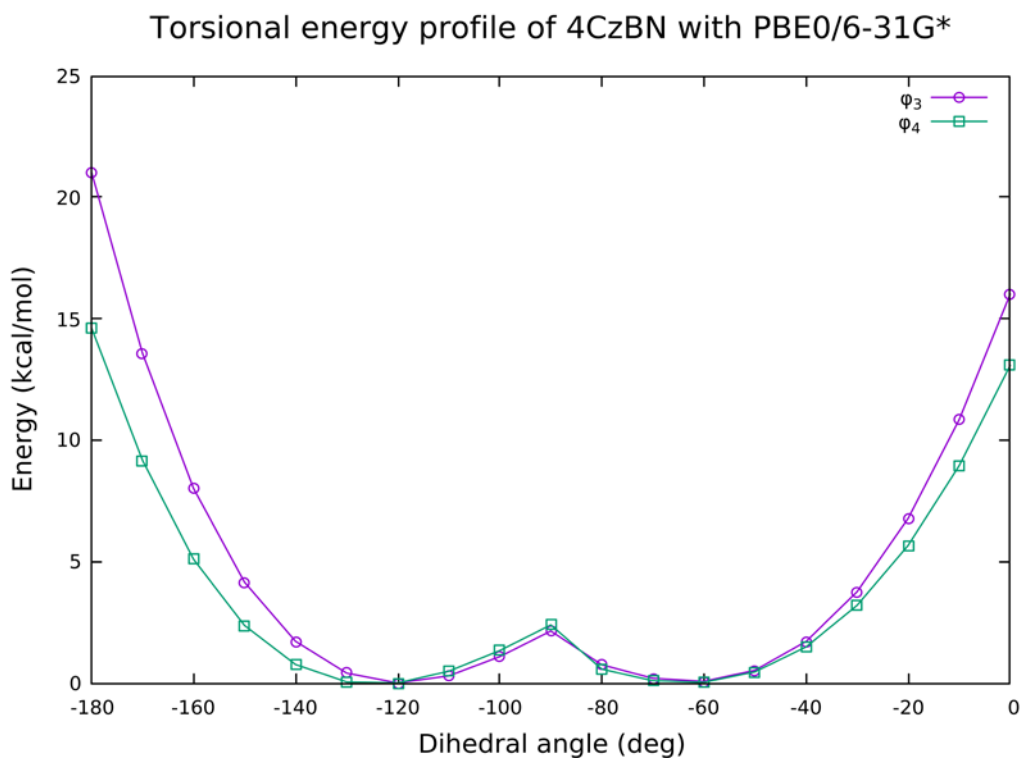
Figure 3.4.4 The potential energy surface relaxed scan of 4CzBN through the dihedral angles φ_3 and φ_4 with the level of calculation PBE0/6-31G*.

We also compare the potential energy scan of 2CzBN and 4CzBN with the same level of calculation PBE0/6-31G*. As it can been seen in figure 3.4.5, in the region of dihedral angle where the relative energies are low φ_4 of 4CzBN has a similar profile to φ_1 of 2CzBN, while φ_3 of 4CzBN gives similar profile to φ_2 of 2CzBN. When steric repulsion is increasing the relative energy of 2CzBN and 4CzBN are a bit different at the same dihedral angle. The similarity between 2CzBN and 4CzBN profiles is an important result as it could allow us using the same molecular mechanics torsional parameters for both molecules in future Molecular Dynamics simulations.

Torsional energy profile of 2CzBN and 4CzBN with PBE0/6-31G*
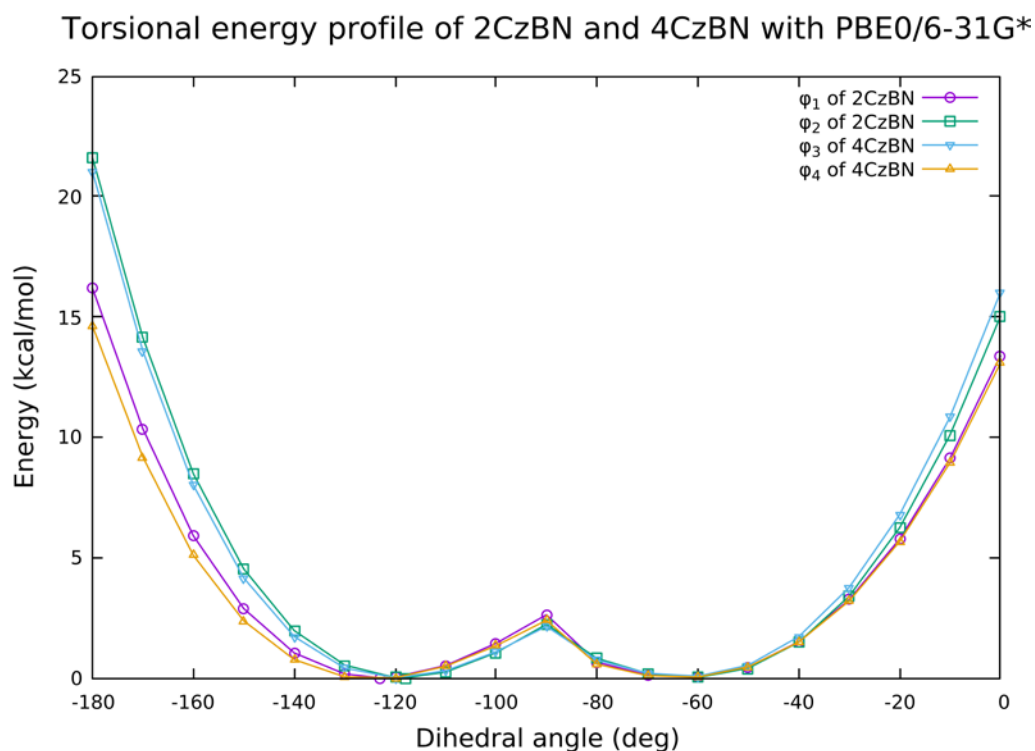
Figure 3.4.5 Comparing the torsional energy profile between 2CzBN and 4CzBN with the level of calculation PBE0/6-31G*.

The optimized conformations of the first excited state and triplet state with respect to φ_2 are also computed. We started with the optimized first singlet excited state (S$_1$) of 2CzBN with TD-PBE0/6-31G* level of calculation. The S$_1$ potential energy surface of 2CzBN was computed keeping fixed one dihedral angle (φ_2) while letting the other one relax (φ_1). The dihedral angle was scanned from 0º to -180º like for the S$_0$ profile. The T$_1$ potential energy surface scan was also computed with open-shell restricted ground state, PBE0/6-31G* (equivalent to TD-PBE0/6-31G*). The potential energy profile of S$_1$ and T$_1$ are shown in figure 3.4.6 where the new Franck-Condon point of S$_0$→S$_1$ is -90º. The carbazole ring is rotating when its ring is almost perpendicular to benzonitrile ring, leading the lower energy in S$_1$ state. On the other hand, the T$_1$ energy profile is similar to S$_0$ energy profile where the Franck-Condon points of S$_0$→T$_1$ are located at ±60º and ±120º.

Torsional energy profile of φ_2 of 2CzBN
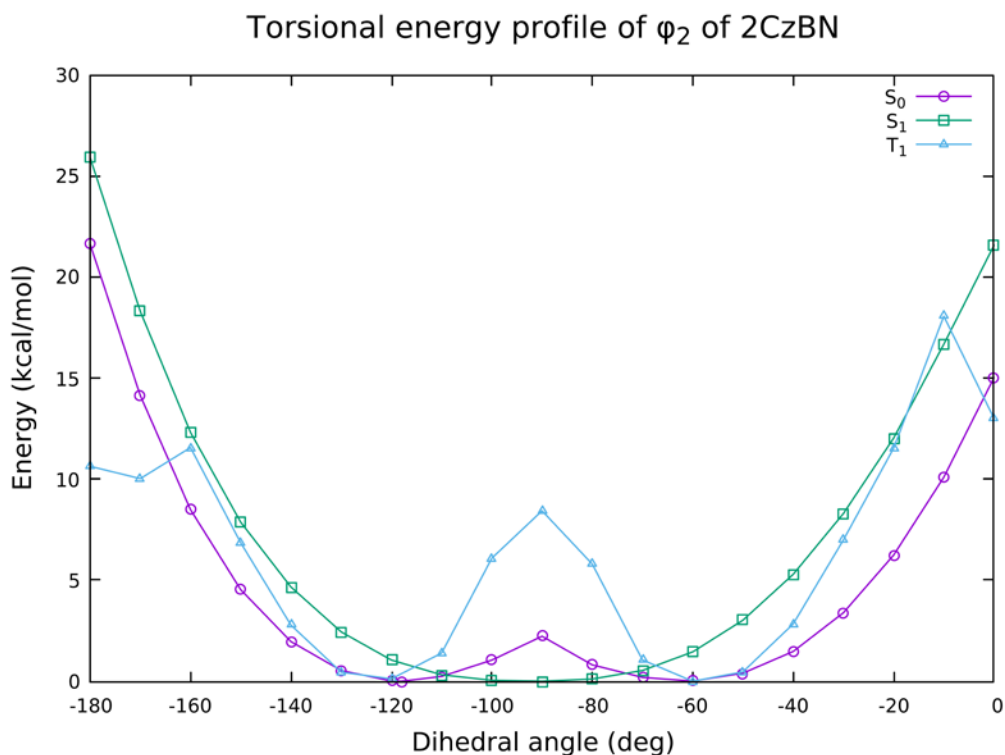
Figure 3.4.6 Comparison of the PES profiles of φ_2 of 2CzBN for S_0 and S_1 optimized geometries with the level of calculation PBE0/6-31G* and TD-PBE0/6-31G* respectively.

3.5 Mapping of calculated state energies and oscillator strengths

The conformation of 2CzBN and 4CzBN was then mapped through DFT calculations carried out fixing both dihedral angles (φ_1 and φ_2), to calculate state energies and oscillator strengths at different conformations. The calculation was first performed at PBE0/3-21G level. It was then improved with the double zeta basis set 6-31G*. The potential energy scan map of ground state of 2CzBN was scanned from -30 degree to -150 degree while fixing both dihedral angles. The results are shown in figures 3.5.1 (for 2CzBN) and 3.5.2 (for 4CzBN), where two global minima appear at both dihedral angles of ~ -60° and -120°. These two global minima conformers can be thermally accessible one from another due to the relatively low energy at the saddle point on the map (φ_1 = -90° and φ_2 = -90°), for which the energy barrier is approximately 4 kcal/mol either in 2CzBN or 4CzBN.
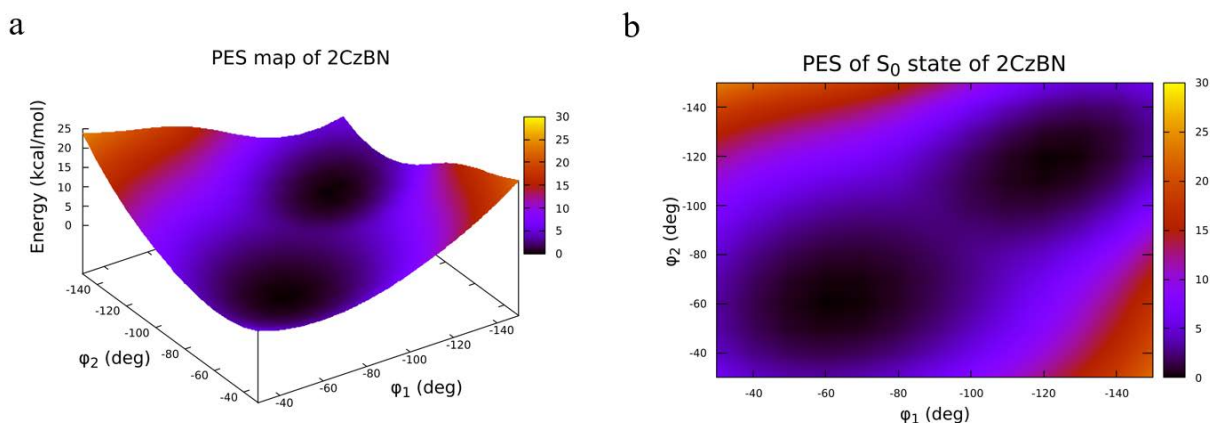
Figure 3.5.1 The potential energy surface scan of 2CzBN through the fixed dihedral angles φ_1 and φ_2 with PBE0/6-31G* (a) side view (b) top view.
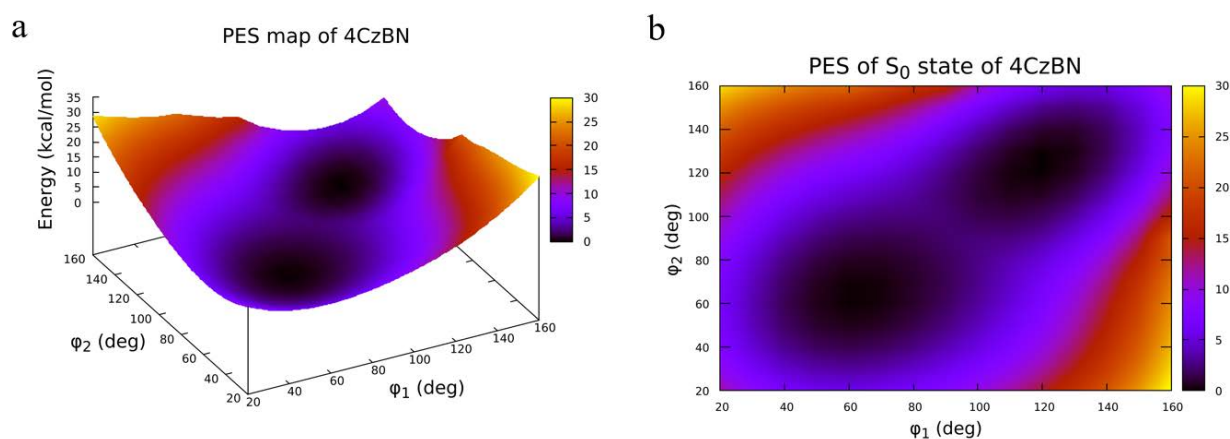
Figure 3.5.2 The potential energy surface scan of 4CzBN through the fixed dihedral angles φ_1 and φ_2 with PBE0/6-31G* (a) side view (b) top view.

The TD-DFT potential energy maps of excited states were also computed with single point TD-PBE0/6-31G* calculations carried out at the optimized ground states geometries. The map of vertical energy gap between S_1 and T_1 state are computed and the ΔE^{ST} map of 2CzBN and 4CzBN are given in figure 3.5.3. The lower region of ΔE^{ST} in both compounds is located at the middle of the map when carbazole ring is almost perpendicular to benzonitrile ring. Therefore, the lower region of ΔE^{ST} is not close to the Franck-Condon points ($\varphi_1 = \varphi_2 = -60^o$ or -120°), but it can be thermally accessible, since the PES of T_1 state in figure 3.5.4 and 3.5.5 shows that this region is a saddle point with an energy barrier of $6 \sim$ kcal/mol.
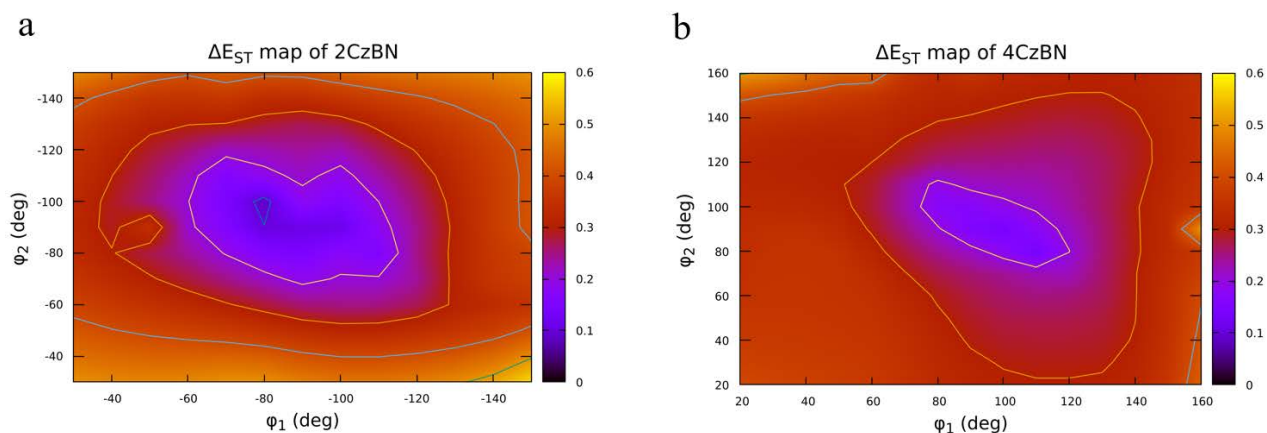
Figure 3.5.3. The ΔE^{ST} (eV) at PBE0/6-31G* level a) 2CzBN b) 4CzBN.

The potential energy map of S_1 and T_1 excited state at the optimized ground state geometries, are shown respectively in figure 3.5.4 and 3.5.5. Both 2CzBN and 4CzBN gave similar results: the lowest energy of S_1 state is achieved when both carbazole rings are almost perpendicular with respect to the benzonitrile moiety. On the other hand, the PES of T_1 is similar to the potential energy profile of the optimized ground state (shown in figure 3.5.1 and 3.5.2 before). The highest energy in S_1 and T_1 occurs when the steric strain of both carbazole rings is maximum. The lower region of ΔE^{ST} is located in between the two Franck-Condon points, precisely at the saddle point in optimized ground state map. Reaching on T_1 the region of lower vertical ΔE^{ST} is thermally possible but unlikely, since the difference between the lowest energy and saddle point in T_1 is approximately 5 kcal/mol.
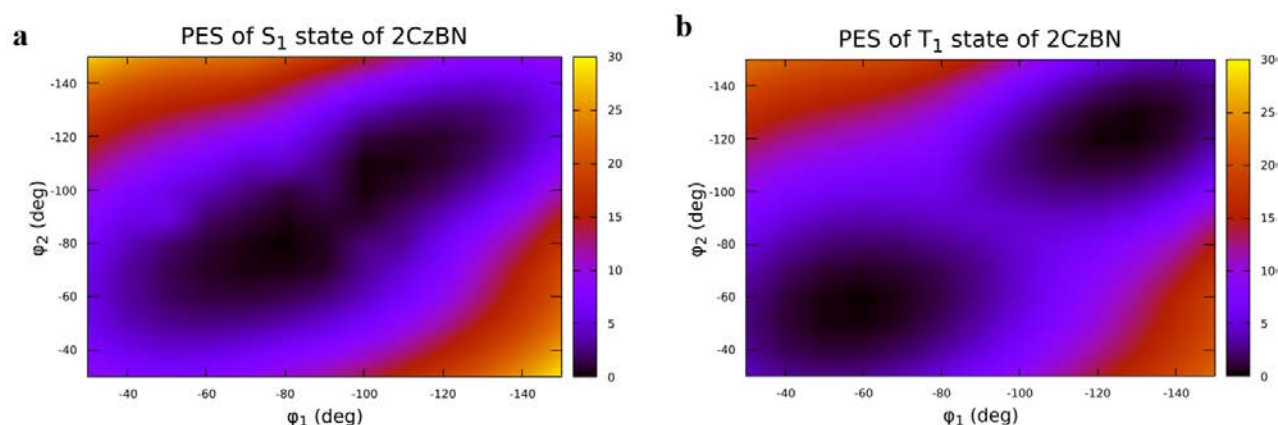
Figure 3.5.4. The potential energy of excited state (kcal/mol) of 2CzBN at PBE0/6-31G* level with respect to optimized ground state geometries: a) energy map of first singlet state and b) energy map of first triplet state.
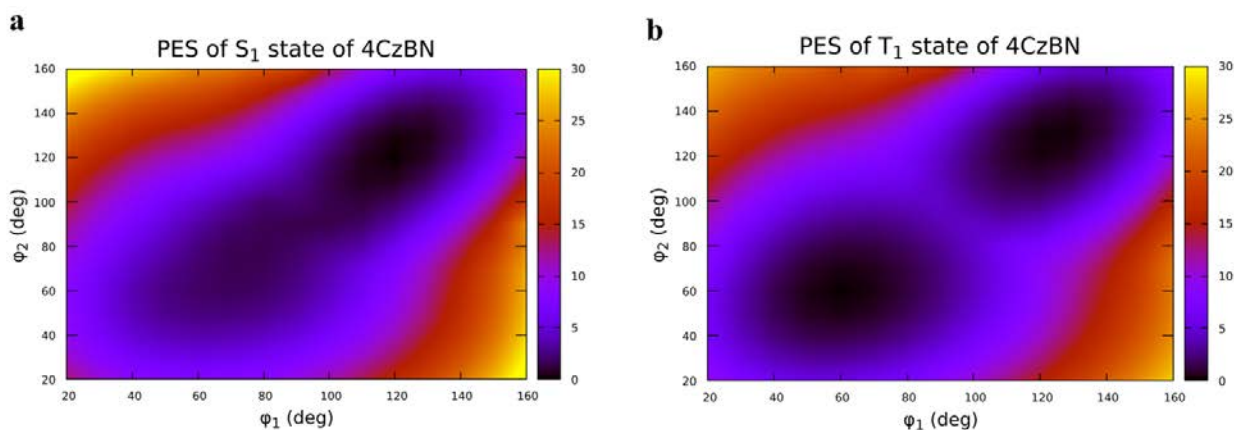
Figure 3.5.5. The potential energy of excited state (kcal/mol) of 4CzBN at PBE0/6-31G* level with respect to optimized ground state geometries: a) energy map of first singlet state and b) energy map of first triplet state.

As we are mainly interested in the emission from the first excited state to the ground state, the corresponding oscillator strength (O.S.) map of 2CzBN was also constructed. In figure 3.5.6a, the O.S. of $S_0 \rightarrow S_1$ is very low in the whole explored region. This result may be in agreement with the experimental results from Adachi and co-worker where 2CzBN is found to be an inactive TADF molecule. For 4CzBN the O.S. is also low, but much higher than for 2CzBN. The problem of low oscillator strength arises from the small overlap between the HOMO and LUMO, leading to suppression of the oscillator strength.
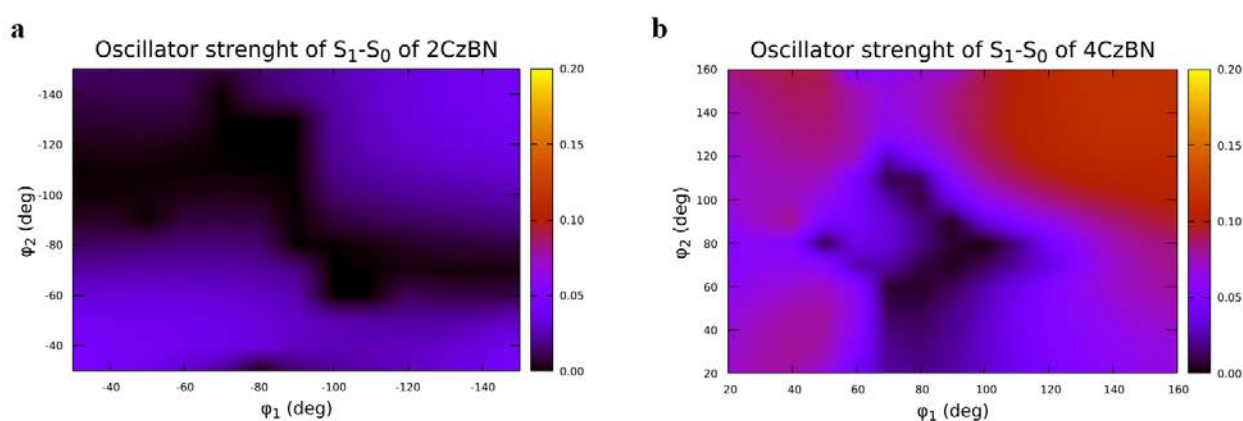
Figure 3.5.6 The oscillator strength map of first excited singlet state (S_1) of a) 2CzBN and b) 4CzBN.

Chapter 4

Characterization of the nature of excited states and of their crossing

To understand and rationalize the efficiency of the TADF process, it is very useful to characterize the nature of excited states which are involved in. To this end, the development of matrics based on charge density is particularly suitable to quickly classify the charge transfer (CT) or locally excited (LE) character of a state. In this section, we characterize the nature of excited state by performing the post-processing in order to quantitively determine the nature of the calculated excited states. The spatial separation of the frontier orbitals was characterized by a metric based on the hole and electron distance Δr (equation 4.3). Also, the overlap between the attachment and detachment density matrices were calculated by using equation 4.2. The two matrices are calculated by using the NANCY EX package[30].

The detachment and attachment density matrices are given by $\boldsymbol{\Gamma}$ and $\boldsymbol{\Lambda}$[31]. For a given electronic transition between two states, it is possible to define two three dimensional function ϱ_τ and ϱ_A representative of the spatial distribution of the electronic density removed (detachment) from the initial state and reorganized (attachment) in the final one during the transition (figure 4.1)[31].

The integration of charge density of detachment (ϱ_τ) or attachment (ϱ_A) through the three-dimensional space gives the total charge (the number of electrons) ϑ_τ involved in the transition, typically one:

$$\boldsymbol{\vartheta_\tau} = \int_R d\xi_1 \int_R d\xi_2 \int_R d\xi_3 \varrho_\tau(\xi_1\xi_2\xi_3) \equiv \int_{R^3} d^3\xi\varrho_\tau(\xi) \qquad (4.1)$$

$$\tau \equiv \boldsymbol{\Gamma, \Lambda}$$
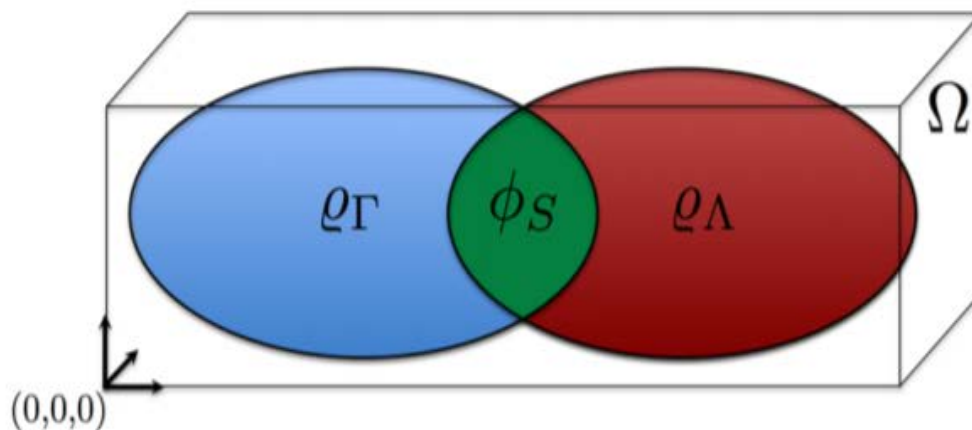
Figure 4.1 Graphical depiction of the ϕ_S descriptor as the overlap between detachment and attachment densities. Figure adapted from reference [30].

A dimensionless parameter ϕ_S can be then defined as the overlap between the attachment and detachment densities. Following equation 4.2, the ϕ_S index can range from 0 to 1, depending on CT character of the electronic transition.

$$\phi_S = \vartheta^{-1} \int_{R^3} d^3\xi \sqrt{\varrho_\Gamma(\xi)\varrho_\Lambda(\xi)} \qquad (4.2)$$

$$\phi_S \in [1:0]$$

where ϑ is the average charge contained in the attachment and detachment charge density functions. The product $\varrho_\Gamma(\xi)\varrho_\Lambda(\xi)$ will be different from zero only in the regions in which there is overlap between the two charge distributions (green region in figure 4.1), so that the highest values of ϕ_S are obtained when the transition results in a zero photoinduced electronic density change (LE), while low values indicate that there is no overlap between detachment and attachment densities (CT transition)[30].

Therefore, ϕ_S quantitatively represents the charge separation nature of a chromophore upon light absorption.

It can be interesting to quantitively provide the coefficient-weighted hole-electron distance (Δr) between a set of orbital centroids. The hole−electron pair interactions could be related to the distance covered during the excitations, so it can be calculated by following equation.

$$\Delta r = \frac{\sum_{ia} K_{ia}^2 |\langle \varphi_a | r | \varphi_a \rangle - \langle \varphi_i | r | \varphi_i \rangle|}{\sum_{ia} K_{ia}^2} \qquad (4.3)$$

where $K_{ia} = X_{ia} + Y_{ia}$ (X_{ia} and Y_{ia} are excitation and de-excitation coefficients produced by the TDDFT calculation), $\langle \varphi_i | r | \varphi_i \rangle$ is the norm of an occupied orbital centroid and $\langle \varphi_a | r | \varphi_a \rangle$ is the norm of virtual orbital centroid[32]. Also, through the value of Δr it can be quantified the nature of an excited state either with charge transfer ($\Delta r \geq 2.0\ A°$) or local excitation ($\Delta r \leq 2.0\ A°$) character. However, if two acceptors are disposed (nearly) symmetrically around a single donor (e.g. in the case of 4CzBN), even a long-range charge-transfer transition can result in $\Delta r \approx 0$, a disadvantage which makes the metrics ϕ_S superior to Δr.

Prior to the calculation of the metrics, the reorganization of the electron density upon electronic transition to the excited states at the ground state geometry was analyzed through the visualization of the attachment and detachment density. For the transition from the S_0 state to S_1, 2CzBN and 4CzBN qualitatively show a CT character (detachment and attachment densities localized in different part of the molecule in figure 4.2a and 4.3a), while the S_0 to T_1 transition shows the LE character (figure 4.2b and 4.3b). The S_0-S_2 transition also exhibit a CT character as in the S_1 state. Interestingly, T_2 state of 2CzBN shows a strong LE character, while T_2 state of 4CzBN shows a mixed character, in between CT and LE (figure 4.4).
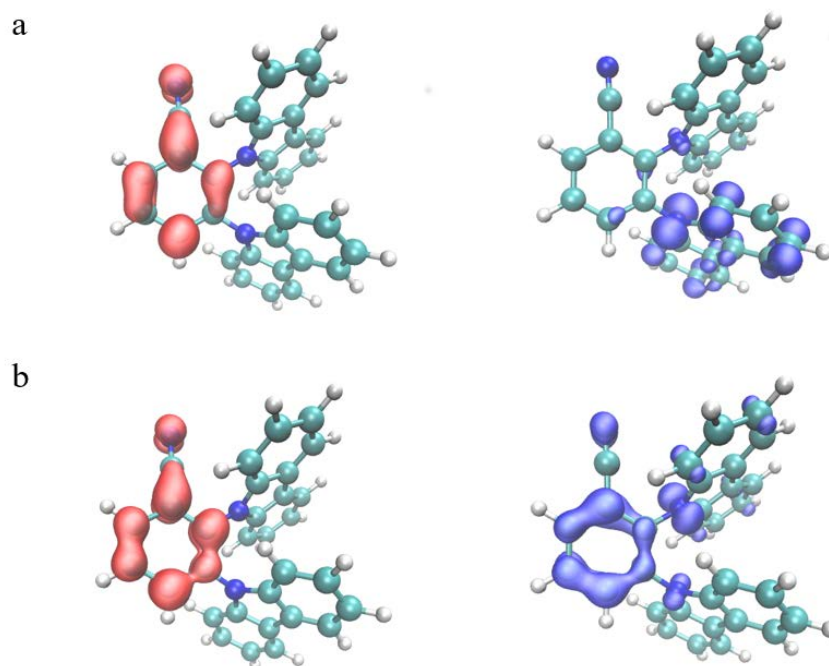
Figure 4.2 Electron (red isocontour) and hole (blue isocontour) densities of 2CzBN obtained in the attachment/detachment formalism from TD-PBE0/6-31G(d,p) calculations ($\varphi_1 = -120^o$, $\varphi_2 = -120^o$) S_0-S_1 transition a) and S_0-T_1 transition b)
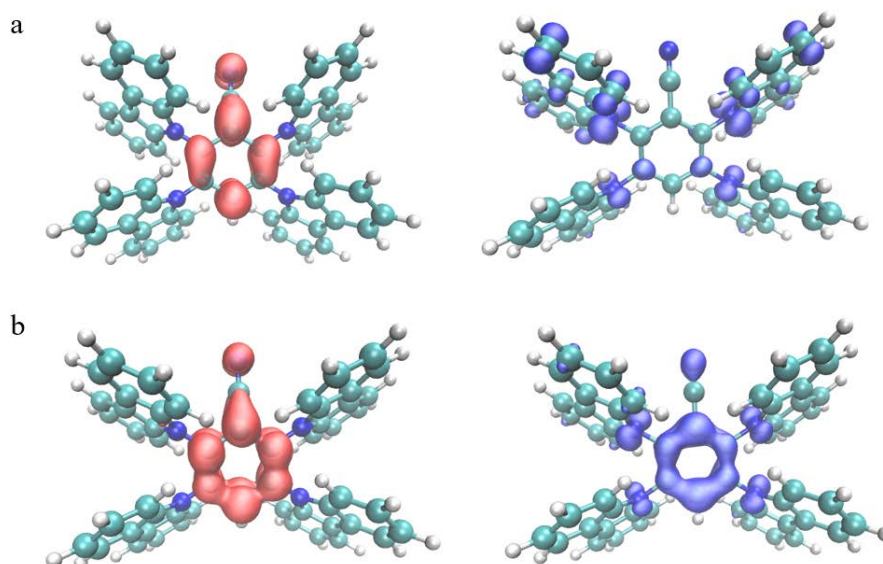
Figure 4.3 Electron (red isocontour) and hole (blue isocontour) densities of 4CzBN obtained in the attachment/detachment formalism from TD-PBE0/6-31G(d,p) calculations ($\varphi_1 = 120^o$, $\varphi_2 = 120^o$) S_0-S_1 transition a) and S_0-T_1 transition b)
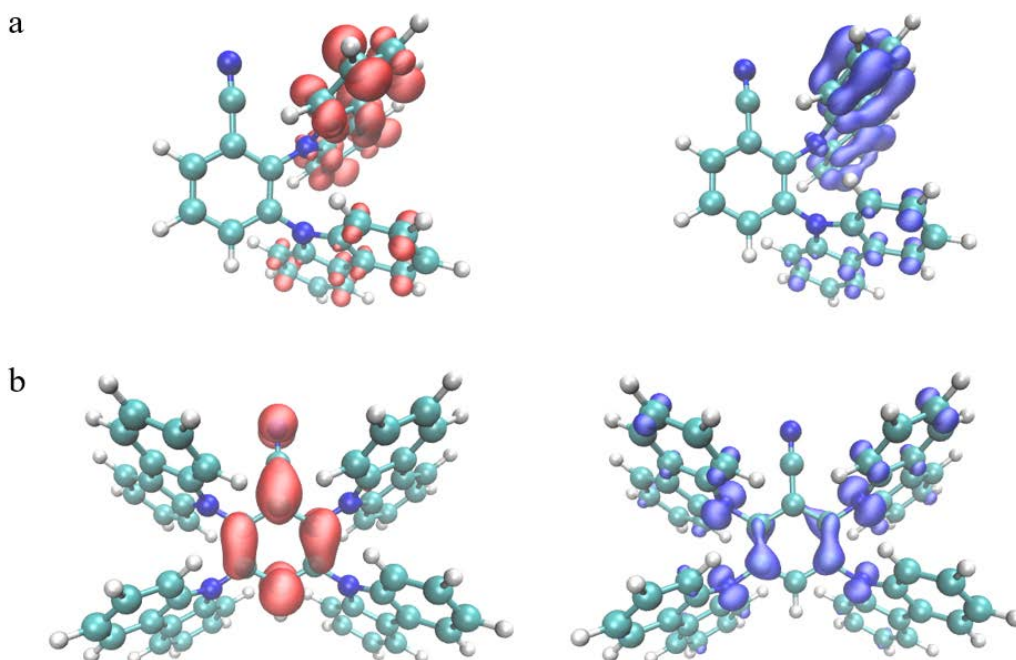
Figure 4.4 Electron (red isocontour) and hole (blue isocontour) densities from S_0 to T_2 obtained in the attachment/detachment formalism from TD-PBE0/6-31G(d,p) calculations ($\varphi_1 = 120^\circ$, $\varphi_2 = 120^\circ$ for 4CzBN and $\varphi_1 = -120^\circ$, $\varphi_2 = -120^\circ$ for 2CzBN) 2CzBN a) and 4CzBN b)

We also quantitively characterized the nature of excited states by defining CT(LE) character with Δr largely above 2.0 Å (close to 0 Å) and ϕ_s close to 0 (1). The values in table 4.1 confirm that S_1 and S_2 exhibit a CT character, while T2 shows the strong a LE character. It can be noticed that Δr of 4CzBN does not follow the criterion that $\Delta r \geq 2.0$ Å for charge transfer character and $\Delta r \leq 2.0$ Å for locally excitation character. This is because of the symmetric D-A-D architecture, when the hole and electron distance are calculated by orbital centroid. In fact, as the D-A-D structure has a symmetry between A unit, consequently the hole and electron centroid are close together. Therefore, Δr cannot be used to quantify the nature of excited state for D-A-D system. We also noticed that the energy of T_2 state is close to that of T_1 state in both compounds (approximately 0.06-0.09 eV), and lower than the S_1 energy, therefore also T_2 could play a role in the TADF process. However, T_2 has a different nature in 2CzBN and 4CzBN, and this could be one of the reasons why 4CzBN is a TADF active emitter, while 2CzBN is not.

Table 4.1 Excited state characterization of 2CzBN of 4CzBN ($\varphi_1 = -120^\circ$, $\varphi_2 = -120^\circ$) where the values of ϕ_S, Δr and nature of excited state are shown in the table. Note that the oscillator strength is only defined for singlet excitation.

	State	E (eV)	O.S.	ϕ_S	Δr (Å)	CT/LE
2CzBN	S_1	3.2745	0.0301	0.34	3.24	CT
	S_2	3.4107	0.0006	0.31	3.86	CT
	T_1	2.9706		0.82	1.26	LE
	T_2	3.0691		0.95	0.09	LE
4CzBN	S_1	2.9865	0.1029	0.40	0.21	CT
	S_2	3.1895	0.0091	0.40	0.53	CT
	T_1	2.7387		0.83	0.07	LE
	T_2	2.8014		0.48	0.25	CT/LE

We also calculated the ϕ_S map of excited states at other geometries in order to determine the variation of excited states with respect to possible conformational changes induced by temperature. These calculations, reported in figure 4.5, confirm that S_1 and S_2 of 2CzBN exhibit a CT characters, while T_1 exhibits a LE character, and as well as T_2 even more markedly in every conformations of molecule.
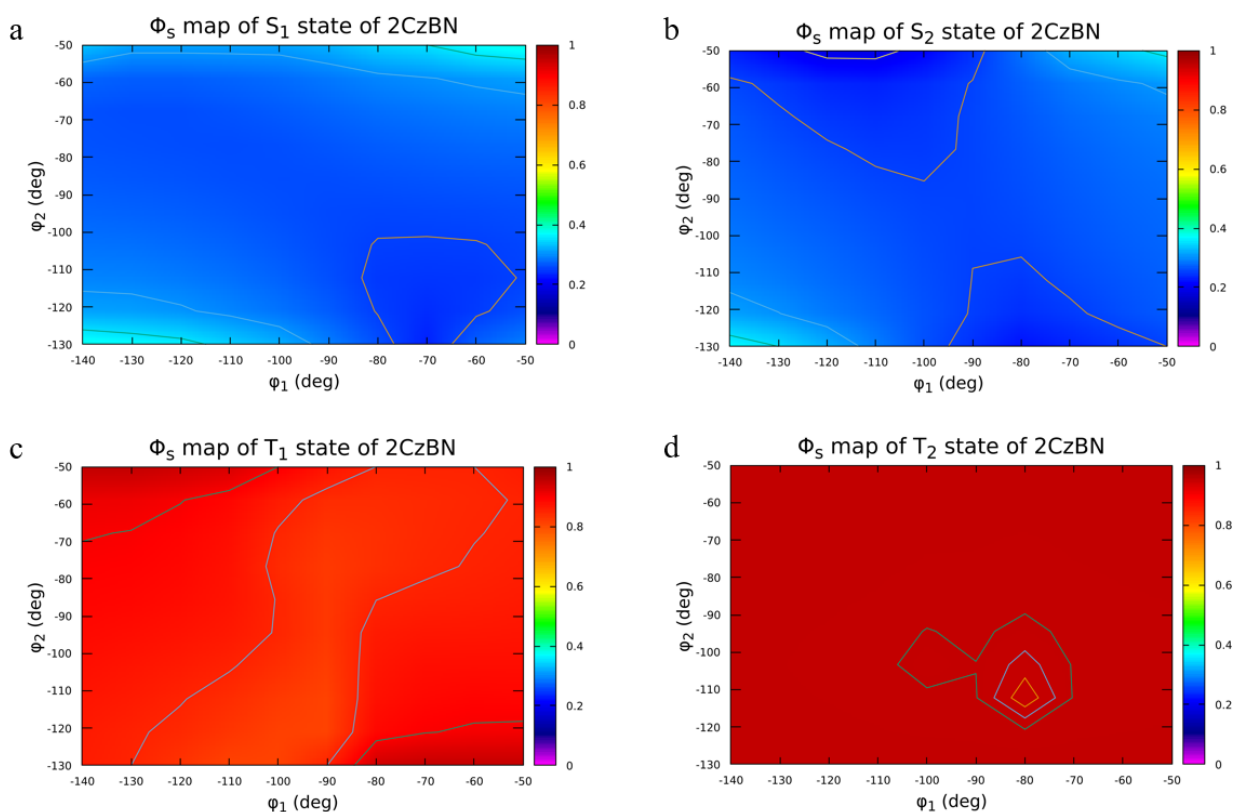
Figure 4.5 ϕ_S map of 2CzBN a) S_0-S_1 transition b) S_0-S_2 transition c) S_0-T_1 transition, and d) S_0-T_2 transition.

For 4CzBN (figure 4.6), the ϕ_S shows that S_1 and S_2 state still exhibit as a CT character, but less than for 2CzBN molecule. On the other hand, the T_1 state shows LE character as in 2CzBN. Interestingly, T_2 state exhibits a mixing character between CT and LE. More in general, the nature of the states of 2CzBN is robust with respect to conformational changes, while for 4CzBN the variations of the singlet states are a bit larger, even if not dramatic.
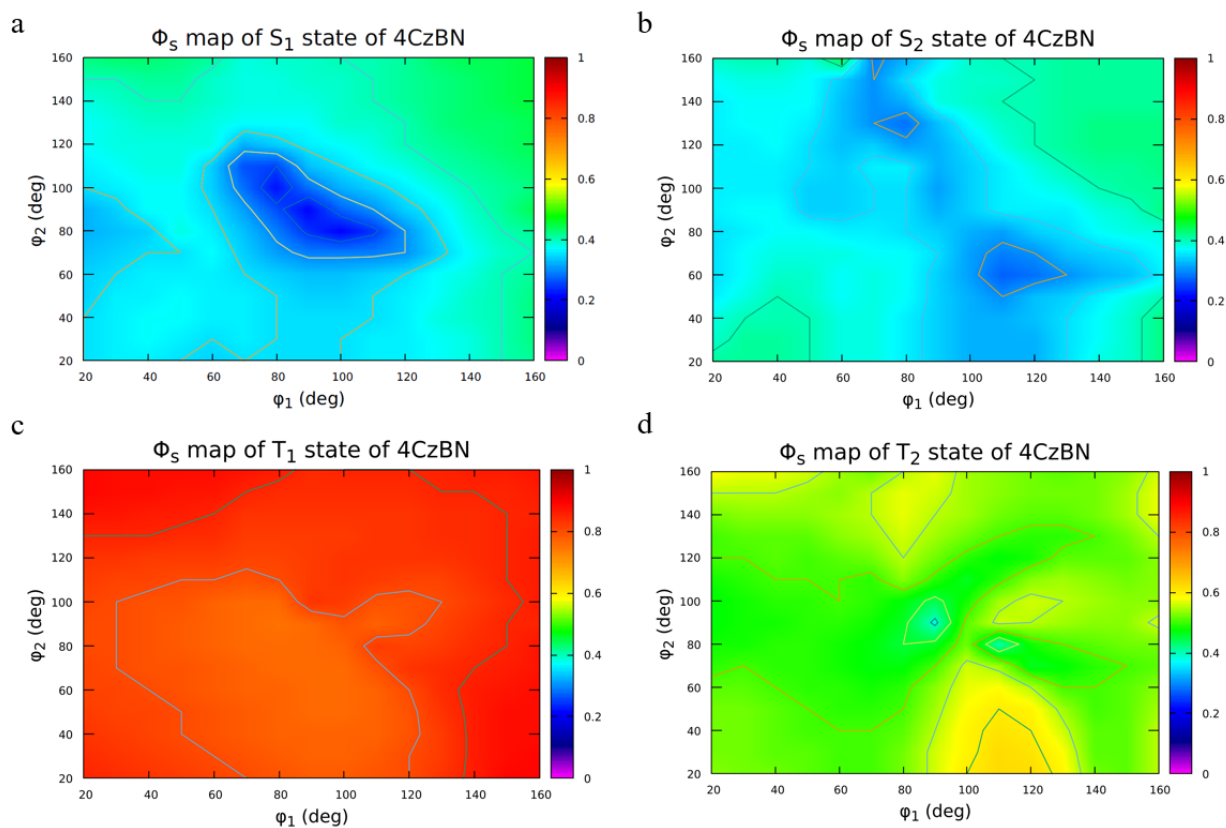
Figure 4.6 ϕ_S map of 4CzBN a) S_0-S_1 transition b) S_0-S_2 transition c) S_0-T_1 transition, and d) S_0-T_2 transition

In the chapter 2, we described how the rate of RISC does not only depend on ΔE_{ST}, but also on the spin-orbit coupling between the involved singlet and triplet states. Therefore, we also calculated the spin-orbit coupling between S_1 and T_1 state using Fermi's golden rule without coupling between electronic and vibrational motion. The spin-orbit coupling elements were calculated using the Breit-Pauli spin-orbit Hamiltonian with effective charge approximation, as implemented in the software pySOC[33]. The latter, in turn, takes as input the wave function files produced by Gaussian LR-TDDFT calculations. The result is shown in figure 4.7. As it can be seen in the maps, SOC between S_1 and T_1 state of 4CzBN is a bit higher than for 2CzBN, another hint towards a more effective TADF process for the former molecule.

a

SOC (meV) between S_1 and T_1 of 2CzBN

b

SOC (meV) between S_1 and T_1 of 4CzBN
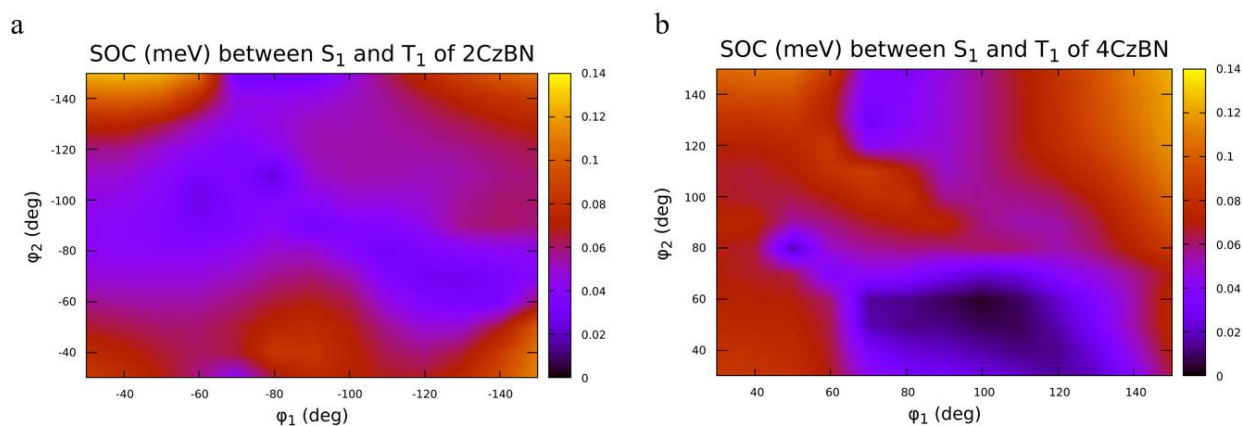
Figure 4.7 Spin-orbit coupling constant (meV) map between S_1 and T_1 states of 2CzBN and 4CzBN with TD-PBE0/6-31G*.

As we mentioned above, the closeness in energy between T_1 and T_2 states, and also the fact that T_2 is lying lower than S_1 state, may play an important role in carbazole-benzonitrile system for TADF performance. To support this possibility, the spin-orbit coupling between S_1 and T_2 state was also computed and shown in figure 4.8. As we can see, 4CzBN has higher value for spin-orbit coupling in some region on the map, while the spin-orbit coupling of 2CzBN is almost constant in every conformers, but low.

a

SOC (meV) between S_1 and T_2 of 2CzBN

b

SOC (meV) between S_1 and T_2 of 4CzBN
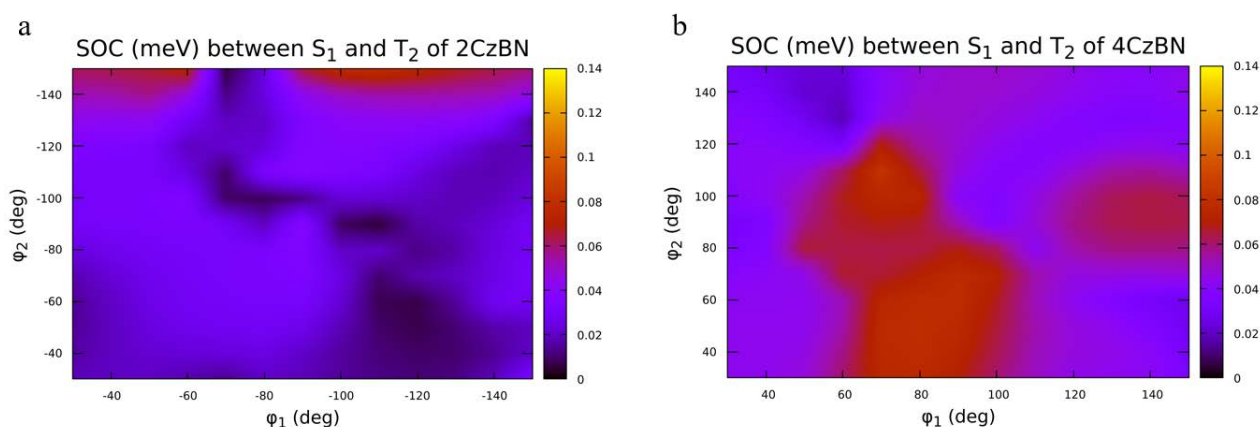
Figure 4.8 Spin-orbit coupling constant (meV) map between S_1 and T_2 state of 2CzBN and 4CzBN with TD-PBE0/6-31G*.

In order to calculate the rate of RISC and ISC with Marcus equation (see Chapter 2 for details),

$$k_{RISC} = \frac{2\pi}{\hbar} V_{SOC}^2 \frac{1}{\sqrt{4\pi\lambda kT}} \exp\left[-\frac{(\lambda + \Delta E_{ST})^2}{4\lambda kT}\right]$$

we need to calculate the reorganization energy (λ) for every transition, as schematized in figure 4.9. The reorganization energy of B state with respect to A can be calculated as E(B) with geometry of A subtracted with the E(B) with geometry of B state.
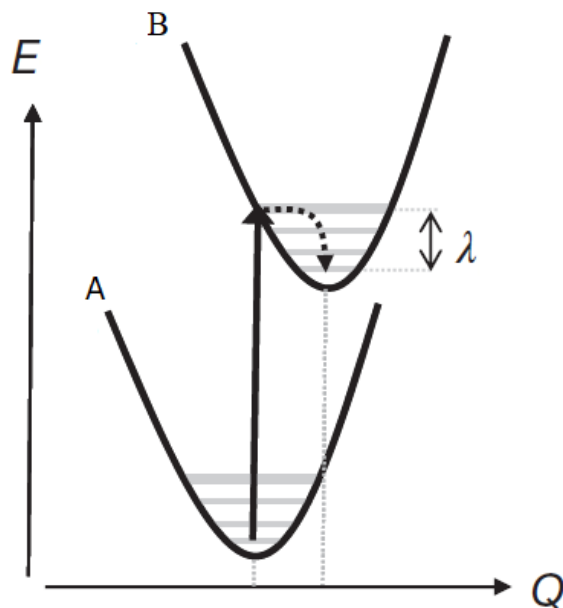
Figure 4.9 Reorganization energy in the final state B upon vertical transition from the initial state A.

The calculated physical parameters are given in table 4.2. We noted that 4CzBN has a rate of RISC, which is the key for TADF performance, higher than 2CzBN. The reverse intersystem crossing process from T_2 to S_1 state has higher rate of RISC than from T_1 to S_1 state. We also noted that the small value of the reorganization energy in 4CzBN is the main parameter increasing the rate of RISC with respect to 2CzBN. The sum of T_1 and T_2 RISC rate of 4CzBN and 2CzBN are $4.23 \times 10^4 \, s^{-1}$ and $1.3 \times 10^3 \, s^{-1}$, respectively. The result shows that the total rate is high enough to drive the TADF process in 4CzBN. The TADF time in 4CzBN shows that it is $2.36 \times 10^{-5} \, s$, while the TADF time of 2CzBN is $7.59 \times 10^{-4} \, s$ which is slower. This can be the reason why 4CzBN is a TADF emitter, but 2CzBN is not a TADF emitter.

Table 4.2 Energy gap between singlet and triplet state (ΔE_{ST}), reorganization energy (λ), spin-orbit coupling (V_{SOC}), rate of Reverse InterSystem Crossing (k_{RISC}) and of Reverse InterSystem Crossing (k_{ISC}) (at equilibrium geometry). All results are obtained from DFT and TD-DFT calculation performed with the PBE0 functional and 6-31G* basis set.

	Transition	ΔE_{ST} (eV)	λ (meV)	V_{SOC} (meV)	Rate	
					k_{RISC} (s^{-1}) x10^5	k_{ISC} (s^{-1}) x 10^8
2CzBN	$S_1 \rightarrow T_1$	-0.304	187	0.440	-	0.565
	$T_1 \rightarrow S_1$	0.304	539	0.440	0.002	-
	$S_1 \rightarrow T_2$	-0.204	87	0.265	-	0.131
	$T_2 \rightarrow S_1$	0.205	539	0.265	0.011	-
Total rate					0.013	0.696
TADF time (s)					7.69×10^{-4}	
4CzBN	$S_1 \rightarrow T_1$	-0.248	221	0.628	-	2.097
	$T_1 \rightarrow S_1$	0.248	249	0.628	0.131	-
	$S_1 \rightarrow T_2$	-0.185	83	0.298	-	0.236
	$T_2 \rightarrow S_1$	0.185	249	0.298	0.292	-
Total rate					0.423	2.33
TADF time (s)					2.36×10^{-5}	

Chapter 5

Conclusions and future outlook

In this work we have theoretically studied, by means of density functional theory (DFT) and TD-DFT calculations, the 2CzBN and 4CzBN (carbazole benzonitrile derivatives) and addressed the question of how a flexible donor-acceptor (D-A) or a linear donor-acceptor-donor (D-A-D) molecular architecture affects the thermally activated delayed fluorescence (TADF) through the nature of excited states, the oscillator strength and the reverse intersystem crossing rates, as a function of the conformation of the carbazole side groups and considering the S_0, S_1, T_1 and T_2 electronic states. We focused in particular on two prototypical molecules, 2CzBN and 4CzBN, that possess a similar energy gap between singlet and triplet (ΔE^{ST}) but still they have different TADF performances. We confirmed that the absorption spectrum of 4CzBN is red-shifted and narrower, compared to that of 2CzBN, owning to a more extended delocalization of the frontier orbitals on the carbazole moieties. The calculated values of vertical ΔE^{ST} of 2CzBN and 4CzBN in gas phase (or including an implicit solvation model for toluene) are 0.30 eV and 0.25 eV (0.28 eV and 0.22 eV), in good agreement with the experimental values of 0.21 eV and 0.22 eV[18], respectively. The torsional energy scans for the rotation of a carbazole group about the carbazole-benzonitrile bond give similar profiles for both compounds in ground state, and slightly different in S_1 and T_1 states. The torsional energy maps considering the simultaneous rotation of two flanked carbazoles show that the energy minima in the ground state are located at 60°, 60° and 120°, 120°, while a saddle point is located at 90°, 90° (when carbazole planes are perpendicular to the benzonitrile ring). Also, the T_1 state profile shares the same minima as the ground state, while in S_1 state the absolute minimum is found at 90°, 90°.

We also investigated the oscillator strength and the nature of excited states, either being of charge transfer (CT) or locally excited (LE) character. The higher oscillator strength of 4CzBN with respect to 2CzBN is one of the factors that contributes to make 4CzBN a TADF active emitter, again as a consequence of larger delocalization of the frontier orbitals involved in the $S_0 \rightarrow S_1$ transition. Both 4CzBN and 2CzBN exhibit a CT character in both S_1 and S_2 states, while T_1 exhibits a LE character. Interestingly, T_2 in 4CzBN shows a mixed character in between CT and LE, while in 2CzBN is strongly a LE character. We also found that the energy of T_2 is always below that of S_1 state, a strong argument supporting the involvement of this further state, besides T_1, in TADF process.

The spin-orbit couplings (V_{SOC}) and reorganization energies (λ) were calculated in order to determine the rate of (Reverse) InterSystem crossing, which is the rate determining-step in TADF based-OLEDs. The rate of RISC of 4CzBN from T_2 to S_1 is surprisingly high compared to T_1 to S_1, since from EL-Sayed rules, this transition should be less favored for 4CzBN being T_2 (CT/LE) more similar to S_1 (CT) than in 2CzBN (LE, CT). The sum of T_1 and T_2 RISC rate (k_{RISC} is 4.23×10^4 s^{-1} and TADF time is 2.36×10^{-5} s) is high enough to drive the TADF process in 4CzBN, while the total RISC rate in 2CzBN (k_{RISC} is 1.3×10^3 s^{-1} and TADF time is 7.69×10^{-4} s) is quite low. This can be the reason why 2CzBN is not a TADF emitter. The lower reorganization energies in 4CzBN seem to be the dominant factor in determining the higher RISC rate. The summary of TADF mechanism and all the calculated values in gas phase are schematized in figure 5.1 and 5.2.
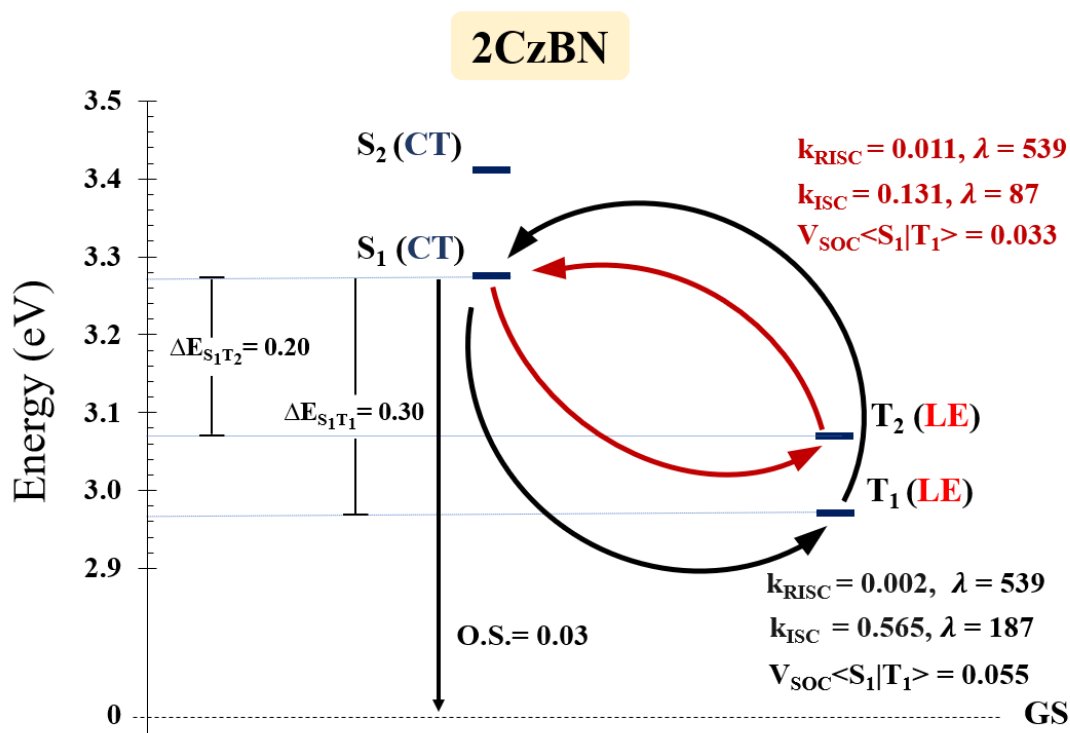
Figure 5.1 The proposed scheme of TADF mechanism in 2CzBN. All the calculation were calculated by means of DFT and TD-DFT calculation with the PBE0/6-31G*. Units: k_{RISC} (s^{-1} $\times 10^5$), k_{ISC} (s^{-1} $\times 10^8$), V_{SOC} (meV) and λ (meV).
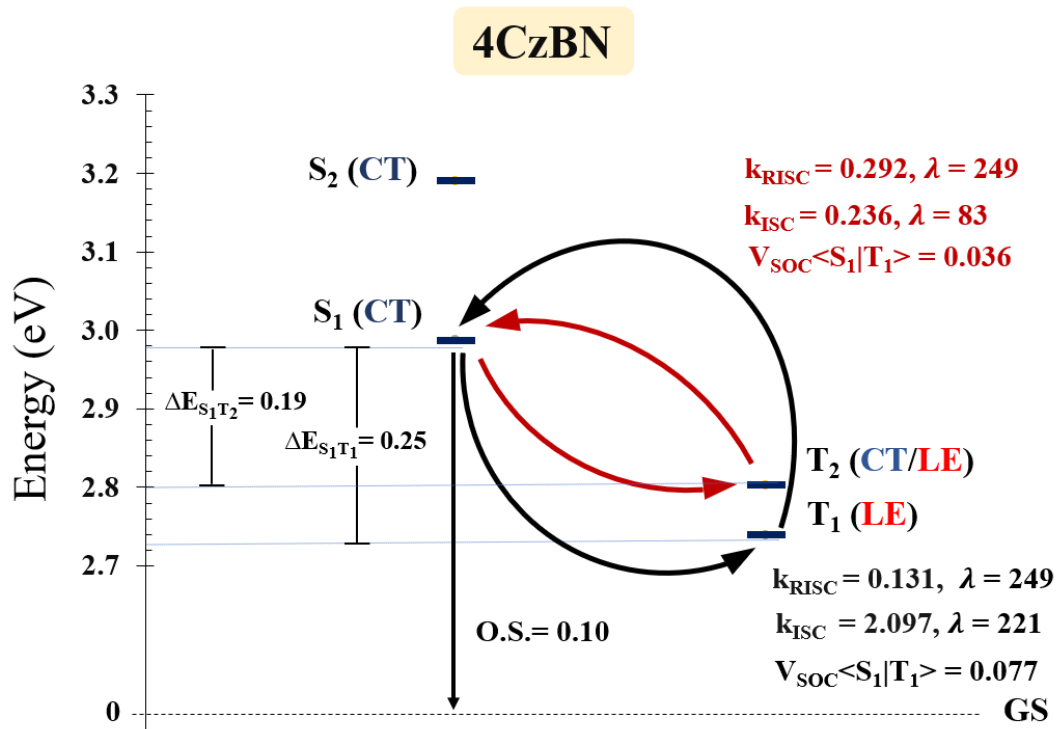
4CzBN

Figure 5.2 The proposed scheme of TADF mechanism in 4CzBN. All the calculation were calculated by means of DFT and TD-DFT calculation with the PBE0/6-31G*. Units: k_{RISC} (s^{-1} $\times10^5$), k_{ISC} (s^{-1} $\times10^8$), V_{SOC} (meV) and λ (meV).

As for outlooks, we noticed that in calculation carried out with implicit solvation model for toluene (the solvent employed in the experiments), the oscillator strength is a bit higher than in gas phase, and ΔE_{ST} gets even closer to the experimental value from Adachi and co-workers[18]. Therefore, taking into account solvent effects could improve the accuracy of the calculation predictions and will be the subject of future investigation.

Bibliography

1. Anna, K. & Heinz, B., Electronic processes in organic semiconductors: An introduction.Wiley (2015).

2. Tang, C. W. & Vanslyke, S. A. Organic electroluminescent diodes. *Appl. Phys. Lett.* **51**, 913–915 (1987).

3. Chen, H.-W., Lee, J.-H., Lin, B.-Y., Chen, S. & Wu, S.-T. Liquid crystal display and organic light-emitting diode display: present status and future perspectives. *Light Sci. Appl.* **7**, 17168 (2018).

4. Nakanotani, H. *et al.* High-efficiency organic light-emitting diodes with fluorescent emitters. *Nat. Commun.* **5**, 1–7 (2014).

5. Lin, L. *et al.* Photo- and electro-luminescence of three TADF binuclear Cu(i) complexes with functional tetraimine ligands. *J. Mater. Chem. C* **5**, 4495–4504 (2017).

6. Minaev, B., Baryshnikov, G. & Agren, H. Principles of phosphorescent organic light emitting devices. *Phys. Chem. Chem. Phys.* **16**, 1719–1758 (2014).

7. Udagawa, K., Sasabe, H., Cai, C. & Kido, J. Low-driving-voltage blue phosphorescent organic light-emitting devices with external quantum efficiency of 30%. *Adv. Mater.* **26**, 5062–5066 (2014).

8. Chihaya, A. Third-generation organic electroluminescence materials. *Jpn. J. Appl. Phys.* **53**, 60101 (2014).

9. Delorme, R. & Perrin, F. Durées de fluorescence des sels d'uranyle solides et de leurs solutions,. *J. Phys. le Radium* **10**, 177–186 (1929).

10. Tao, Y. *et al.* Thermally activated delayed fluorescence materials towards the breakthrough of organoelectronics. *Adv. Mater.* **26**, 7931–7958 (2014).

11. Olivier, Y., Moral, M., Muccioli, L. & Sancho-García, J. C. Dynamic nature of excited states of donor-acceptor TADF materials for OLEDs: How theory can reveal structure-property relationships. *J. Mater. Chem. C* **5**, 5718–5729 (2017).

12. Im, Y. *et al.* Molecular Design Strategy of Organic Thermally Activated Delayed Fluorescence Emitters. *Chem. Mater.* **29**, 1946–1963 (2017).

13. Dias, F. B., Penfold, T. J., Berberan-Santos, M. N. & Monkman, A. P. Photophysics of Thermally Activated Delayed Fluorescence in Organic Molecules. 227–261 (2018).

14. Hosokai, T. *et al.* Solvent-dependent investigation of carbazole benzonitrile derivatives: does the LE3−CT1 energy gap facilitate thermally activated delayed fluorescence? *J. Photonics Energy* **8**, 1 (2018).

15. Chen, T. *et al.* Understanding the Control of Singlet-Triplet Splitting for Organic Exciton Manipulating: A Combined Theoretical and Experimental Approach. *Sci. Rep.* **5**, 1–11 (2015).

16. Dias, F. B. *et al.* The role of local triplet excited states and D-A relative orientation in thermally activated delayed fluorescence: Photophysics and devices. *Adv. Sci.* **3**, 1–10 (2016).

17. Nobuyasu, R. S. *et al.* The influence of molecular geometry on the efficiency of thermally activated delayed fluorescence. *J. Mater. Chem. C* **7**, 6672–6684 (2019).

18. Hosokai, T. *et al.* Evidence and mechanism of efficient thermally activated delayed fluorescence promoted by Delocalized Excited States. Sci. Adv. 3, e1603282 (2017)

19. Li, S. W. *et al.* Cyanopyrimidine-Carbazole Hybrid Host Materials for High-Efficiency and Low-Efficiency Roll-Off TADF OLEDs. *ACS Appl. Mater. Interfaces* **10**, 12930–12936 (2018).

20. Wex, B. & Kaafarani, B. R. Perspective on carbazole-based organic compounds as emitters and hosts in TADF applications. *J. Mater. Chem. C* **5**, 8622–8653 (2017).

21. Valeur, B. *Molecular Fluorescence: Principles and Applications* **8**, (2001).

22. Bañares, L. Unexpected intersystem crossing. *Nat. Chem.* **11**, 103–104 (2019).

23. Shakeel, U. & Singh, J. Study of processes of reverse intersystem crossing (RISC) and thermally activated delayed fluorescence (TADF) in organic light emitting diodes (OLEDs). *Org. Electron. physics, Mater. Appl.* **59**, 121–124 (2018).

24. Marian, C. M. Spin-orbit coupling and intersystem crossing in molecules. *Wiley Interdiscip. Rev. Comput. Mol. Sci.* **2**, 187–203 (2012).

25. Olivier, Y. *et al.* Nature of the singlet and triplet excitations mediating thermally activated delayed fluorescence. *Phys. Rev. Mater.* **1**, 1–6 (2017).

26. Uoyama, H., Goushi, K., Shizu, K., Nomura, H. & Adachi, C. Highly efficient organic light-emitting diodes from delayed fluorescence. *Nature* **492**, 234–238 (2012).

27. Turro, N. J., Ramamurthy, V. & Scaiano, J. C. Modern Molecular Photochemistry of Organic Molecules. *Photochem. Photobiol.* **88**, 1033–1033 (2012).

28. Foresman, J. & Frisch, Æ. Exploring Chemistry With Electronic Structure Methods.pdf. *Exploring Chemistry with Electronic Structure Methods* 302 (1996).

29. Moral, M., Muccioli, L., Son, W. J., Olivier, Y. & Sancho-Garcia, J. C. Theoretical rationalization of the singlet-triplet gap in oleds materials: Impact of charge-transfer character. *J. Chem. Theory Comput.* **11**, 168–177 (2015).

30. Etienne, T., Assfeld, X. & Monari, A. New insight into the topology of excited states through detachment/attachment density matrices-based centroids of charge. *J. Chem. Theory Comput.* **10**, 3906–3914 (2014).

31. Etienne, T., Assfeld, X. & Monari, A. Toward a quantitative assessment of electronic transitions" charge-transfer character. *J. Chem. Theory Comput.* **10**, 3896–3905 (2014).

32. Guido, C. A., Cortona, P., Mennucci, B. & Adamo, C. On the metric of charge transfer molecular excitations: A simple chemical descriptor. *J. Chem. Theory Comput.* **9**, 3118–3126 (2013).

33. Gao, X. *et al.* Evaluation of Spin-Orbit Couplings with Linear-Response Time-Dependent Density Functional Methods. *J. Chem. Theory Comput.*, **13**, 515−524 (2017)